10 Quantum Chromodynamics (QCD)

This chapter provides an introduction to the theory of Quantum Chromodynamics (QCD). Firstly, the concept of a local gauge symmetry is described and then used to obtain the form of the QCD interaction. Superficially QCD appears like a stronger version of QED with eight gluons replacing the single photon, but because the gluons carry the charge of the interaction, QCD behaves very differently. A number of important topics are discussed including colour confinement, hadronisation, renormalisation, running coupling constants and colour factors. The last part of chapter provides an introduction to hadron–hadron collisions at the Tevatron and the LHC.

10.1 The local gauge principle

Gauge invariance is a familiar idea from electromagnetism, where the physical **E** and **B** fields, which are obtained from the scalar and vector potentials ϕ and **A**, do not change under the gauge transformation

$$\phi \rightarrow \phi' = \phi - \frac{\partial \chi}{\partial t} \quad \text{and} \quad \mathbf{A} \rightarrow \mathbf{A}' = \mathbf{A} + \boldsymbol{\nabla}\chi .$$

This gauge transformation can be written more succinctly as

$$A_\mu \rightarrow A'_\mu = A_\mu - \partial_\mu \chi, \tag{10.1}$$

where $A_\mu = (\phi, -\mathbf{A})$ and $\partial_\mu = (\partial_0, \boldsymbol{\nabla})$.

In relativistic quantum mechanics, the gauge invariance of electromagnetism can be related to a local gauge principle. Suppose there is a fundamental symmetry of the Universe that requires the invariance of physics under *local* phase transformations defined by

$$\psi(x) \rightarrow \psi'(x) = \hat{U}(x)\psi(x) = e^{iq\chi(x)}\psi(x). \tag{10.2}$$

This is similar to the U(1) global phase transformation of $\psi \rightarrow \psi' = e^{i\phi}\psi$ of (9.3), but here the phase $q\chi(x)$ can be different at all points in space-time. For this local U(1) phase transformation, the free-particle Dirac equation

$$i\gamma^\mu \partial_\mu \psi = m\psi, \tag{10.3}$$

becomes

$$\begin{aligned} i\gamma^\mu \partial_\mu (e^{iq\chi(x)}\psi) &= m e^{iq\chi(x)}\psi \\ \Rightarrow \quad e^{iq\chi}\, i\gamma^\mu \left[\partial_\mu \psi + iq(\partial_\mu \chi)\psi\right] &= e^{iq\chi} m\psi \\ i\gamma^\mu (\partial_\mu + iq\partial_\mu \chi)\psi &= m\psi, \end{aligned} \tag{10.4}$$

which differs from (10.3) by the term $-q\gamma^\mu(\partial_\mu \chi)\psi$. Hence, as it stands, the *free-particle* Dirac equation does not possess the hypothesised invariance under a U(1) local phase transformation. More generally, local phase invariance is not possible for a free theory, i.e. one without interactions. The required invariance can be established only by modifying the Dirac equation to include a new degree of freedom A_μ such that the original form of the Dirac equation of (10.3) becomes

$$i\gamma^\mu (\partial_\mu + iqA_\mu)\psi - m\psi = 0, \tag{10.5}$$

where A_μ will be interpreted as the field corresponding to a massless gauge boson. Equation (10.5) is invariant under the local phase transformation defined in (10.2) provided A_μ transforms as

$$A_\mu \to A'_\mu = A_\mu - \partial_\mu \chi,$$

in order to cancel the unwanted $-q\gamma^\mu(\partial_\mu \chi)\psi$ term in (10.4). Stating this another way, for physical predictions to remain unchanged under a local U(1) phase transformation, it is necessary to introduce a new field that exhibits the *observed* gauge invariance of classical electromagnetism, as given in (10.1). More significantly, the modified Dirac equation of (10.5) no longer corresponds to a wave equation for a free particle, there is now an interaction term of the form

$$q\gamma^\mu A_\mu \psi. \tag{10.6}$$

This is identical to the QED interaction term of (5.13) which was previously identified using minimal substitution.

The requirement that physics is invariant under local U(1) phase transformations implies the existence of a *gauge field* which couples to Dirac particles in exactly the same way as the photon. This is a profound statement; all of QED, including ultimately Maxwell's equations, can be derived by requiring the invariance of physics under local U(1) transformations of the form $\hat{U} = e^{iq\chi(x)}$.

10.1.1 From QED to QCD

Quantum Electrodynamics (QED) corresponds to a U(1) local gauge symmetry of the Universe. The underlying symmetry associated with Quantum Chromodynamics (QCD), which is the Quantum Field Theory of the strong interaction, is invariance under SU(3) local phase transformations,

$$\psi(x) \to \psi'(x) = \exp\left[ig_S\,\boldsymbol{\alpha}(x)\cdot\hat{\mathbf{T}}\right]\psi(x). \tag{10.7}$$

Here $\hat{\mathbf{T}} = \{T^a\}$ are the eight generators of the SU(3) symmetry group, which are related to the Gell-Mann matrices of (9.31) by

$$T^a = \tfrac{1}{2}\lambda^a,$$

and $\alpha^a(x)$ are eight functions of the space-time coordinate x. Because the generators of SU(3) are represented by 3×3 matrices, the wavefunction ψ must now include three additional degrees of freedom that can be represented by a three component vector analogous to the representation of the u, d and s quarks in SU(3) flavour symmetry. This new degree of freedom is termed "colour" with red, blue and green labelling the states. The SU(3) local phase transformation corresponds to "rotating" states in this colour space about an axis whose direction is different at every point in space-time. For the local gauge transformation of (10.7), the Dirac equation becomes

$$i\gamma^\mu\left[\partial_\mu + ig_S(\partial_\mu\boldsymbol{\alpha})\cdot\hat{\mathbf{T}}\right]\psi = m\psi. \tag{10.8}$$

The required local gauge invariance can be asserted by introducing eight new fields $G_\mu^a(x)$, where the index $a = 1, \ldots, 8$, each corresponding to one of the eight generators of the SU(3) symmetry. The Dirac equation, including the interactions with the new gauge fields,

$$i\gamma^\mu\left[\partial_\mu + ig_S G_\mu^a T^a\right]\psi - m\psi = 0, \tag{10.9}$$

is invariant under local SU(3) phase transformations provided the new fields transform as

$$G_\mu^k \to G_\mu^{k\prime} = G_\mu^k - \partial_\mu\alpha_k - g_S f_{ijk}\alpha_i G_\mu^j. \tag{10.10}$$

The last term in (10.10) arises because the generators of the SU(3) symmetry do not commute and the f_{ijk} are the *structure constants* of the SU(3) group, defined by the commutation relations $[\lambda_i, \lambda_j] = 2if_{ijk}\lambda_k$. Because the generators SU(3) do not commute, QCD is known as a non-Abelian gauge theory and the presence of the additional term in (10.10) gives rise to gluon self-interactions (see Appendix F). The mathematical forms of these triple and quartic gluon vertices, shown in Figure 10.1, are completely specified by the SU(3) gauge symmetry. Putting aside these self-interactions for now, the required SU(3) local gauge invariance necessitates the modification of the Dirac equation to include new interaction terms, one for each of the eight generators of the gauge symmetry. The eight new fields G^a are

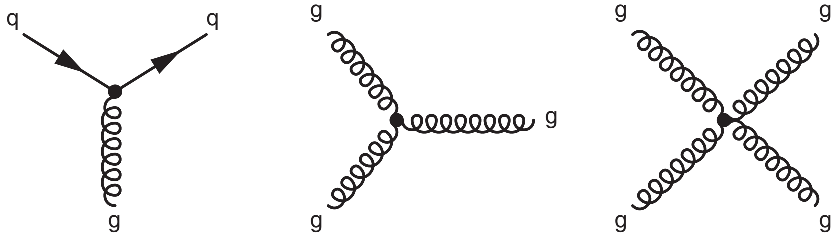

Fig. 10.1 The predicted QCD interaction vertices arising from the requirement of SU(3) local gauge invariance.

the gluons of QCD and from (10.9) it can be seen that the form of qqg interaction vertex is

$$g_S T^a \gamma^\mu G^a_\mu \psi = g_S \tfrac{1}{2}\lambda^a \gamma^\mu G^a_\mu \psi. \tag{10.11}$$

10.2 Colour and QCD

The underlying theory of quantum chromodynamics appears to be very similar to that of QED. The QED interaction is mediated by a massless photon corresponding to the single generator of the U(1) local gauge symmetry, whereas QCD is mediated by eight massless gluons corresponding to the eight generators of the SU(3) local gauge symmetry. The single charge of QED is replaced by three conserved "colour" charges, r, b and g (where colour is simply a label for the orthogonal states in the SU(3) colour space). Only particles that have non-zero colour charge couple to gluons. For this reason the leptons, which are colour neutral, do not feel the strong force. The quarks, which carry colour charge, exist in three orthogonal colour states. Unlike the approximate SU(3) flavour symmetry, discussed in Chapter 9, the SU(3) colour symmetry is exact and QCD is invariant under unitary transformations in colour space. Consequently, the strength of QCD interaction is independent of the colour charge of the quark. In QED the antiparticles have the opposite electric charge to the particles. Similarly, in QCD the antiquarks carry the opposite colour charge to the quarks, $\bar{r}$, $\bar{g}$ and $\bar{b}$.

The three colour states of QCD can be represented by colour wavefunctions,

$$r = \begin{pmatrix} 1 \\ 0 \\ 0 \end{pmatrix}, \quad g = \begin{pmatrix} 0 \\ 1 \\ 0 \end{pmatrix} \quad \text{and} \quad b = \begin{pmatrix} 0 \\ 0 \\ 1 \end{pmatrix}.$$

Following the discussion of SU(3) flavour symmetry in Chapter 9, the colour states of quarks and antiquarks can be labelled by two additive quantum numbers, the

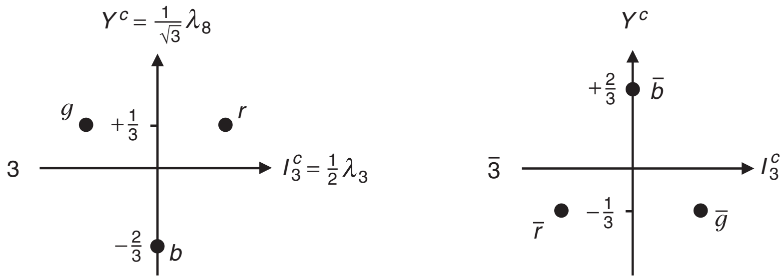

Fig. 10.2 The representations of the colour of quarks and the anticolour of antiquarks.

third component of colour isospin I_3^c and colour hypercharge Y^c as indicated in Figure 10.2.

10.2.1 The quark–gluon vertex

The SU(3) local gauge symmetry of QCD implies a conserved colour charge and an interaction between quarks and gluons of the form given by (10.11). By comparing the QCD interaction term to that for QED given in (10.6),

$$-iq\gamma^\mu A_\mu \psi \to -ig_S \tfrac{1}{2}\lambda^a \gamma^\mu G_\mu^a \psi,$$

the QCD vertex factor can be identified as

$$-iq\gamma^\mu \to -ig_S \gamma^\mu \tfrac{1}{2}\lambda^a.$$

Apart from the different coupling constant, the quark–gluon interaction only differs from the QED interaction in the appearance of the 3 × 3 Gell-Mann matrices that only act on the colour part of the quark wavefunction. The quark wavefunctions therefore need to include this colour degree of freedom. This can be achieved by writing

$$u(p) \to c_i u(p),$$

where $u(p)$ is a Dirac spinor and c_i represents one of the possible colour states

$$c_1 = r = \begin{pmatrix} 1 \\ 0 \\ 0 \end{pmatrix}, \quad c_2 = g = \begin{pmatrix} 0 \\ 1 \\ 0 \end{pmatrix} \quad \text{and} \quad c_3 = b = \begin{pmatrix} 0 \\ 0 \\ 1 \end{pmatrix}.$$

Consequently, the quark current associated with the QCD vertex, shown in Figure 10.3, can be written

$$j_{\mathrm{q}}^\mu = \overline{u}(p_3) c_j^\dagger \left\{ -\tfrac{1}{2} i g_S \lambda^a \gamma^\mu \right\} c_i u(p_1), \tag{10.12}$$

where the c_i and c_j are the colour wavefunctions of the quarks and the index a refers to gluon corresponding to the SU(3) generator T^a. (In other textbooks you may see the colour index appended to the spinor $c_i u(p) \to u_i(p)$.)

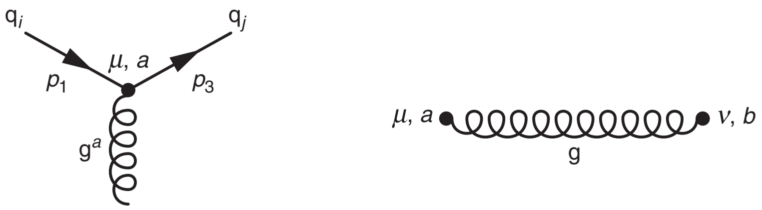

Fig. 10.3 The QCD quark–gluon vertex representing the interaction of quarks with colours *i* and *j* with a gluon of type *a* and the gluon propagator.

In the quark current of (10.12), the 3 × 3 Gell-Mann matrix λ^a acts on the three-component colour wavefunction, whereas the 4 × 4 γ-matrices act on the four components of the Dirac spinor. Therefore the colour part of the current factorises, allowing (10.12) to be written as

$$\overline{u}(p_3)c_j^\dagger\{-\tfrac{1}{2}ig_s\lambda^a\gamma^\mu\}c_i u(p_1) = -\tfrac{1}{2}ig_s\left[c_j^\dagger\lambda^a c_i\right]\times\left[\overline{u}(p_3)\gamma^\mu u(p_1)\right].$$

The factorised colour part of the interaction is

$$c_j^\dagger\lambda^a c_i = c_j^\dagger\begin{pmatrix}\lambda^a_{1i}\\ \lambda^a_{2i}\\ \lambda^a_{3i}\end{pmatrix} = \lambda^a_{ji}.$$

Hence the qqg vertex can be written as

$$-\tfrac{1}{2}ig_S\,\lambda^a_{ji}\left[\overline{u}(p_3)\gamma^\mu u(p_1)\right],$$

where λ^a_{ji} is just a number, namely the jith element of λ^a. Therefore, the Feynman rule associated with the QCD vertex is

$$-\tfrac{1}{2}ig_S\,\lambda^a_{ji}\gamma^\mu.$$

For lowest-order diagrams, the Feynman rule for the gluon propagator of Figure 10.3 is

$$-i\frac{g_{\mu\nu}}{q^2}\delta^{ab},$$

where the delta-function ensures that the gluon of type a emitted at the vertex labelled μ is the same as that which is absorbed at vertex ν.

10.3 Gluons

The QCD interaction vertex includes a factor λ^a_{ji}, where i and j label the colours of the quarks. Consequently, gluons corresponding to the non-diagonal Gell-Mann

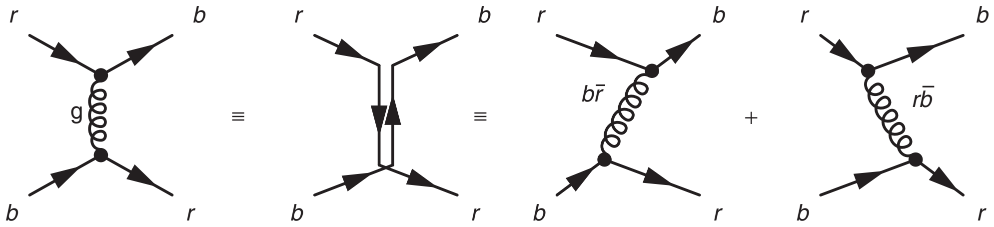

Fig. 10.4 Colour flow for the t-channel process $rb \to br$. Shown as the Feynman diagram, the colour flow and the two time-ordered diagrams.

matrices connect quark states of different colour. In order for colour to be conserved at the interaction vertex, the gluons must carry colour charge. For example, the gluon corresponding to λ_4, defined in (9.31), which has non-zero entries in the 13 and 31 positions, contributes to interactions involving the changes of colour $r \to b$ and $b \to r$. This is illustrated in Figure 10.4, which shows the QCD process of qq → qq scattering where the colour flow corresponds to $br \to rb$, illustrated both in terms the colour flow in the Feynman diagram and as the two corresponding time-ordered diagrams. Because colour is a conserved charge, the interaction involves the exchange of a $b\bar{r}$ gluon in the first time-ordering and a $r\bar{b}$ gluon in the second time-ordering. From this discussion, it is clear that gluons must carry simultaneously both colour charge and anticolour charge.

Since gluons carry a combination of colour and anticolour, there are six gluons with different colour and anticolour, $r\bar{g}$, $g\bar{r}$, $r\bar{b}$, $b\bar{r}$, $g\bar{b}$ and $b\bar{g}$. Naïvely one might expect three gluons corresponding to $r\bar{r}$, $g\bar{g}$ and $b\bar{b}$. However, the physical gluons correspond to the fields associated with the generators $\lambda_{1,...,8}$ of the SU(3) gauge symmetry. The gluons are therefore an octet of coloured states, analogous to the $\mathrm{q\bar{q}}$ meson SU(3) flavour states. The colour assignments of the eight physical gluons can be written

$$r\bar{g},\ g\bar{r},\ r\bar{b},\ b\bar{r},\ g\bar{b},\ b\bar{g},\ \tfrac{1}{\sqrt{2}}(r\bar{r}-g\bar{g}) \quad \text{and} \quad \tfrac{1}{\sqrt{6}}(r\bar{r}+g\bar{g}-2b\bar{b}).$$

Even though two of these gluon states have $I_3^c = Y^c = 0$, they are part of a colour octet and therefore still carry colour charge (unlike the colourless singlet state).

10.4 Colour confinement

There is a wealth of experimental evidence for the existence of quarks. However, despite many experimental attempts to detect free quarks, which would be observed as fractionally charged particles, they have never been seen directly. The non-observation of free quarks is explained by the hypothesis of *colour confinement*, which states that coloured objects are always confined to colour singlet states and

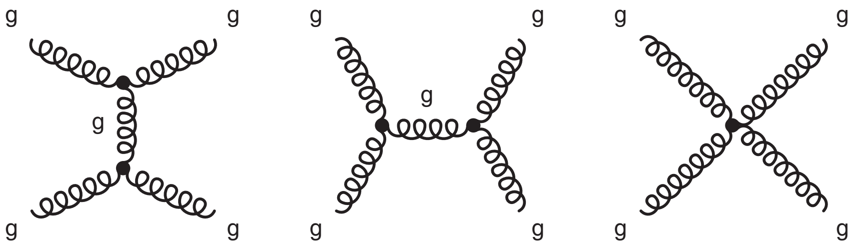

Fig. 10.5 Lowest-order Feynman diagrams for the process gg ⟶ gg, formed from the triple and quartic gluon vertices of Figure 10.1.

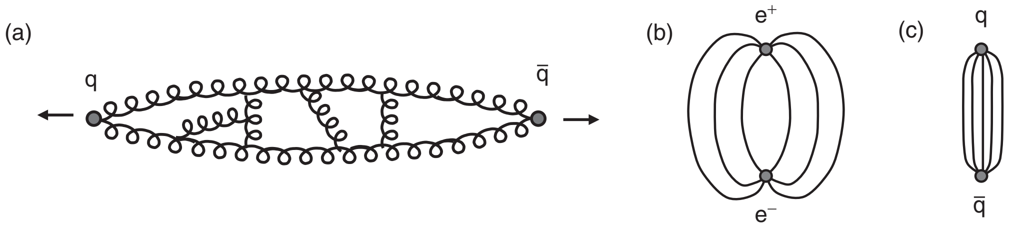

Fig. 10.6 Qualitative picture of the effect of gluon–gluon interactions on the long-range QCD force.

that no objects with non-zero colour charge can propagate as free particles. Colour confinement is believed to originate from the gluon–gluon self-interactions that arise because the gluons carry colour charge, allowing gluons to interact with other gluons through diagrams such as those shown in Figure 10.5.

There is currently no analytic proof of the concept of colour confinement, although there has been recent progress using the techniques of lattice QCD. Nevertheless, a qualitative understanding of the likely origin can be obtained by considering what happens when two free quarks are pulled apart. The interaction between the quarks can be thought of in terms of the exchange of virtual gluons. Because they carry colour charge, there are attractive interactions between these exchanged virtual gluons, as indicated in Figure 10.6a. The effect of these interactions is to squeeze the colour field between the quarks into a tube. Rather than the field lines spreading out as in QED (Figure 10.6b), they are confined to a tube between the quarks, as indicated in Figure 10.6c. At relatively large distances, the energy density in the tube between the quarks containing the gluon field is constant. Therefore the energy stored in the field is proportional the separation of the quarks, giving a term in the potential of the form

$$V(\mathbf{r}) \sim \kappa \mathrm{r}, \tag{10.13}$$

where experimentally $\kappa \sim 1\,\mathrm{GeV/fm}$. This experimentally determined value for κ (see Section 10.8) corresponds to a very large force of $\mathcal{O}(10^5)\,\mathrm{N}$ between *any* two unconfined quarks, regardless of separation! Because the energy stored in the colour field increases linearly with distance, it would require an infinite amount of energy to separate two quarks to infinity. Put another way, if there are two free colour charges in the Universe, separated by macroscopic distances, the energy stored in the resulting gluon field between them would be vast. As a result, coloured objects arrange themselves into bound hadronic states that are colourless combinations with no colour field between them. Consequently quarks are always confined to colourless hadrons.

Another consequence of the colour confinement hypothesis is that gluons, being coloured, are also confined to colourless objects. Therefore, unlike photons (the force carriers of QED), gluons do not propagate over macroscopic distances. It is interesting to note that had nature chosen a U(3) local gauge symmetry, rather than SU(3), there would be a ninth gluon corresponding to the additional U(1) generator. This gluon would be the colour singlet state,

$$G_9 = \frac{1}{\sqrt{3}}(r\bar{r} + g\bar{g} + b\bar{b}).$$

Because this gluon state is colourless, it would be unconfined and would behave like a strongly interacting photon, resulting in an infinite range strong force; the Universe would be a very different (and not very hospitable) place with long-range strong interactions between all quarks.

10.4.1 Colour confinement and hadronic states

Colour confinement implies that quarks are always observed to be confined to bound colourless states. To understand exactly what is meant by "colourless", it is worth recalling the states formed from the combination of spin for two spin-half particles. The four possible spin combinations give rise to a triplet of spin-1 states and a spin-0 singlet ($2 \otimes 2 = 3 \oplus 1$):

$$|1,+1\rangle = \uparrow\uparrow,\ \ |1,0\rangle = \frac{1}{\sqrt{2}}(\uparrow\downarrow + \downarrow\uparrow),\ \ |1,-1\rangle = \downarrow\downarrow \ \ \text{and}\ \ |0,0\rangle = \frac{1}{\sqrt{2}}(\uparrow\downarrow - \downarrow\uparrow).$$

The singlet state is "spinless" in the sense that it carries no angular momentum. In a similar way, SU(3) colour singlet states are colourless combinations which have zero colour quantum numbers, $I_3^c = Y^c = 0$. It should be remembered that $I_3^c = Y^c = 0$ is a necessary but not sufficient condition for a state to be colourless. The action of any of the SU(3) colour ladder operators on a colour singlet state must yield zero, in which case the state is analogous to the spinless $|0,0\rangle$ singlet state.

The colour confinement hypothesis implies that only colour singlet states can exist as free particles. Consequently, all bound states of quarks and antiquarks must occur in colour singlets. This places a strong restriction on the structure of possible hadronic states; the allowed combinations of quarks and antiquarks are those where a colour singlet state can be formed. The algebra of the exact SU(3) colour symmetry was described in Chapter 9 in the context of SU(3) flavour symmetry and the results can be directly applied to colour with the replacements, u → r, d → g and s → b.

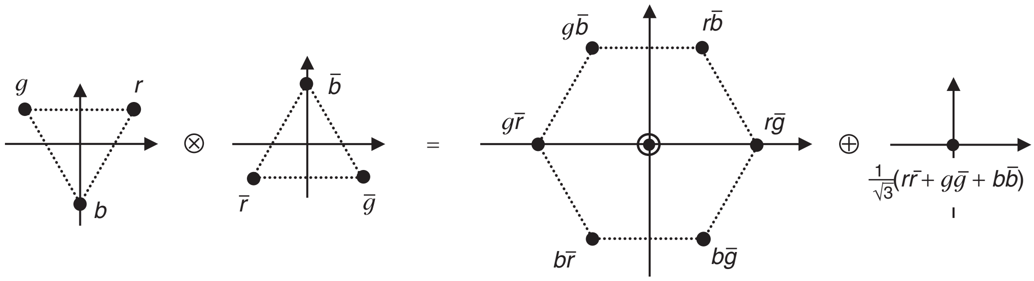

Fig. 10.7 The colour combination of a quark and an antiquark, $3 \otimes \bar{3} = 8 \oplus 1$.

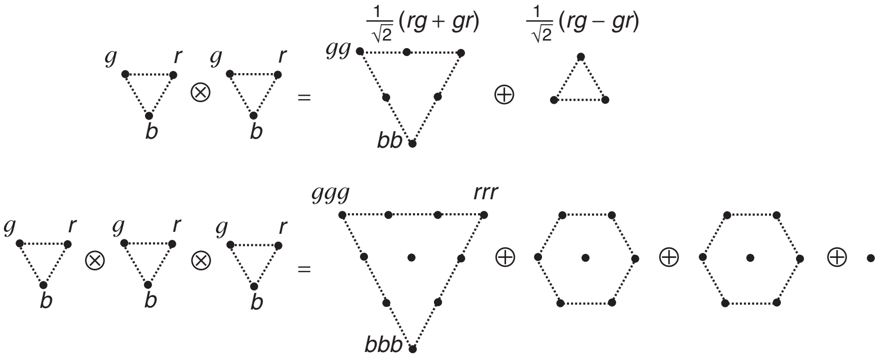

Fig. 10.8 The multiplets from the colour combinations of two quarks, $3 \otimes 3 = 6 \oplus \bar{3}$, and three quarks, $3 \otimes 3 \otimes 3 = 10 \oplus 8 \oplus 8 \oplus 1$.

First consider the possible colour wavefunctions for a bound $q\bar{q}$ state. The combination of a colour with an anticolour is mathematically identical to the construction of meson *flavour* wavefunctions in SU(3) flavour symmetry. The resulting colour multiplets, shown in Figure 10.7, are a coloured octet and a colourless singlet. The colour confinement hypothesis implies that all hadrons must be colour singlets, and hence the colour wavefunction for mesons is

$$\psi^c(q\bar{q}) = \frac{1}{\sqrt{3}}(r\bar{r} + g\bar{g} + b\bar{b}).$$

The addition of another quark (or antiquark) to either the octet or singlet state in Figure 10.7 will not yield a state with $I_3^c = Y^c = 0$. Therefore, it can be concluded that bound states of $qq\bar{q}$ or $q\bar{q}\,\bar{q}$ do not exist in nature.

These arguments can be extended to the combinations of two and three quarks as shown in Figure 10.8. The combination of two colour triplets yields a colour sextet and a colour triplet ($\bar{3}$). The absence of a colour singlet state for the qq system, implies that bound states of two quarks are always coloured objects and therefore do not exist in nature. However, the combination of three colours yields a single singlet state with the colour wavefunction

$$\psi^c(\mathrm{qqq}) = \tfrac{1}{\sqrt{6}}(rgb - rbg + gbr - grb + brg - bgr), \tag{10.14}$$

analogous to the SU(3) flavour singlet wavefunction of Section 9.6.4. This state clearly satisfies the requirement that $I_3^c = Y^c = 0$. The colour ladder operators can be used to confirm it is a colour singlet. For example, the action of the colour isospin raising operator T_+^c, for which $T_+^c g = r$, gives

$$T_+^c \psi^c(\mathrm{qqq}) = \tfrac{1}{\sqrt{6}}(rrb - rbr + rbr - rrb + brr - brr) = 0,$$

as required. Hence a SU(3) colour singlet state can be formed from the combination of three quarks and colourless bound states of qqq are observed in nature. Since the colour singlet wavefunction of (10.14) is totally antisymmetric, and it is the only colour singlet state for three quarks, the colour wavefunction for baryons is always antisymmetric. This justifies the assumption used in Chapter 9 to construct the baryon wavefunctions.

Colour confinement places strong restrictions on the possible combinations of quarks and antiquarks that can form bound hadronic states. To date, all confirmed observed hadronic states correspond to colour singlets either in the form of mesons ($\mathrm{q\overline{q}}$), baryons (qqq) or antibaryons ($\mathrm{\overline{q}\,\overline{q}\,\overline{q}}$). In principle, combinations of ($\mathrm{q\overline{q}}$) and (qqq) such as pentaquark states ($\mathrm{qqqq\overline{q}}$) could exist, either as bound states in their own right or as hadronic molecules such as ($\mathrm{q\overline{q}}$)-(qqq). In recent years there have been a number of claims for the existence of pentaquark states, but the evidence is (at best) far from convincing.

10.4.2 Hadronisation and jets

In processes such as $\mathrm{e^+e^-} \to \mathrm{q\overline{q}}$, the two (initially free) high-energy quarks are produced travelling back to back in the centre-of-mass frame. As a consequence of colour confinement, the quarks do not propagate freely and are observed as jets of colourless particles. The process by which high-energy quarks (and gluons) produce jets is known as hadronisation.

A qualitative description of the hadronisation process is shown in Figure 10.9. The five stages correspond to: (i) the quark and antiquark produced in an interaction initially separate at high velocities; (ii) as they separate the colour field is restricted to a tube with energy density of approximately 1 GeV/fm; (iii) as the quarks separate further, the energy stored in the colour field is sufficient to provide the energy necessary to form new $\mathrm{q\overline{q}}$ pairs and breaking the colour field into smaller "strings" is energetically favourable; (iv) this process continues and further $\mathrm{q\overline{q}}$ pairs are produced until (v) all the quarks and antiquarks have sufficiently low energy to combine to form colourless hadrons. The hadronisation process results in two jets of hadrons, one following the initial quark direction and the other in the initial antiquark direction. Hence, in high-energy experiments, quarks and gluons

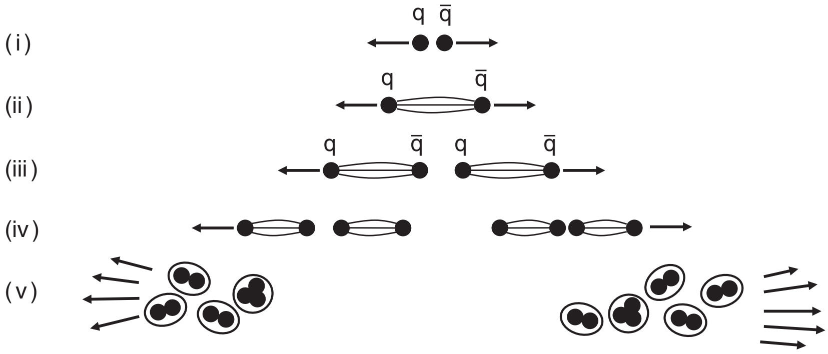

Fig. 10.9 Qualitative picture of the steps in the hadronisation process.

are always observed as jets of hadrons (see for example, Figures 10.19 and 10.30). The precise process of hadronisation is poorly understood. Nevertheless, there are a number of phenomenological models (often with many free parameters) that are able to provide a reasonable description of the experimental data. Whilst these models are motived by QCD, they are a long way from a first-principles theoretical description of the hadronisation process.

10.5 Running of α_S and asymptotic freedom

At low-energy scales, the coupling constant of QCD is large, $\alpha_S \sim \mathcal{O}(1)$. Consequently, the perturbation expansion discussed in the context of QED in Section 6.1, does not converge rapidly. For this reason (low-energy) QCD processes are not calculable using traditional perturbation theory. Nevertheless, in recent years, there has been a significant progress with the computational technique of *lattice QCD*, where quantum-mechanical calculations are performed on a discrete lattice of space-time points. Such calculations are computationally intensive, with a single calculation often taking many months, even using specially adapted supercomputing facilities. With lattice QCD it has been possible to calculate the proton mass with a precision of a few per cent, thus providing a first principles test of the validity of QCD in the non-perturbative regime. Despite this success, most practical calculations in particle physics are based on perturbation theory. For this reason, it might seem problematic that perturbation theory cannot be applied in QCD processes because of the large value of α_S. Fortunately, it turns out that α_S is not constant; its value depends on the energy scale of the interaction being considered. At high energies, α_S becomes sufficiently small that perturbation theory can again be used. In this way, QCD divides into a non-perturbative low-energy regime, where first-principles calculations are not currently possible, such as the hadronisation process, and a high-energy regime where perturbation theory can be used.

The running of α_S is closely related to the concept of renormalisation. A thorough mathematical treatment of renormalisation is beyond the level of this book. Nevertheless, it is necessary to introduce the basic ideas in order to provide a qualitative understanding of the running of the coupling constants of both QED and QCD.

10.5.1 *Renormalisation in QED

The strength of the interaction between a photon and an electron is determined by the coupling at the QED vertex, which up to this point has been taken to be constant with value e. The experimentally measured value of the electron charge e, which corresponds to $\alpha \approx 1/137$, is obtained from measurements of the strength of the static Coulomb potential in atomic physics. This is not the same as the strength of coupling between an electron and photon that appears in Feynman diagrams, which can be written as e_0 (often referred to as the bare electron charge); the experimentally measured value of e is the effective strength of the interaction which results from the sum over all relevant QED higher-order diagrams.

Up to this point, only the lowest-order contribution to the QED coupling between a photon and a charged fermion, shown in Figure 10.10a, has been considered. However, for each QED vertex in a Feynman diagram, there is an infinite set of higher-order corrections; for example, the $\mathcal{O}(e^2)$ corrections to the QED $e^-\gamma e^-$ vertex are shown in Figures 10.10b–10.10e. The experimentally measured strength of the QED interaction is the effective strength from the sum over of all such diagrams. The diagram of Figure 10.10b represents correction to the propagator and the diagrams in Figures 10.10c–10.10e represent corrections to the electron four-vector current. In principle, both types of diagram will modify the strength of the interaction relative to the lowest-order diagram alone.

For each higher-order diagram, it is relatively straightforward to write down the matrix element using the Feynman rules for QED. Each loop in a Feynman diagram enters as an integral over the four momenta of the particles in the loop and such diagrams lead to divergent (infinite) results. Fortunately, the infinities associated with the loop corrections to the photon propagator can be absorbed into the definition of the electron charge (described below). However, the corrections to four-vector

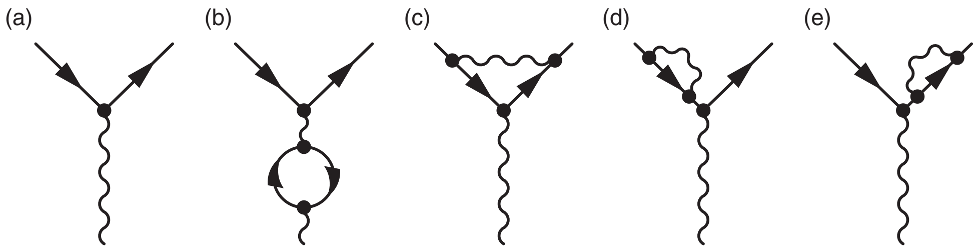

Fig. 10.10 The lowest-order diagram for the QED vertex and the $\mathcal{O}(e^2)$ corrections.

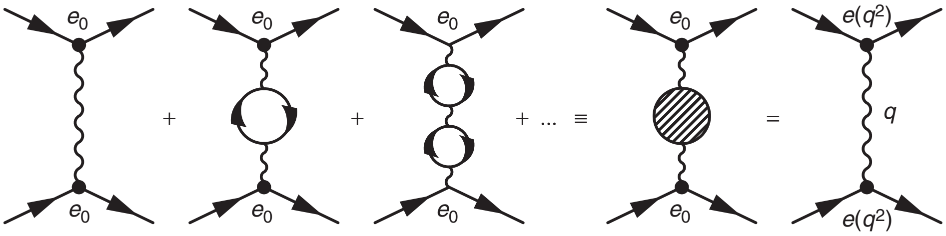

Fig. 10.11 Renormalisation in QED, relating the running charge $e(q^2)$ to the bare charge e_0.

current, Figures 10.10c–10.10e, are potentially more problematic as they involve loops that include virtual fermions. Consequently, the results of the corresponding loop integrals will depend on the fermion masses. In principle, this would result in the effective strength of the QED interaction being dependent on the mass of the particle involved, which is not the case. However, in a field theory with local gauge invariance such as QED, the effect of the diagram of Figure 10.10c is exactly cancelled by the effects of diagrams 10.10d–10.10e. This type of cancellation, that is known as a Ward identity, holds to all orders in perturbation theory. Consequently, here we only need to consider the higher-order corrections to the photon propagator.

The infinite series of corrections to the photon propagator, known as the photon self-energy terms, are accounted for by replacing the lowest-order photon exchange diagram by the infinite series of loop diagrams expressed in terms on the bare electron charge, e_0. As a result of the loop corrections, the photon propagator including the self-energy terms, will no longer have a simple $1/q^2$ form. The physical effects of the modification to the propagator can be accounted for by retaining the $1/q^2$ dependence for the effective propagator and absorbing the corrections into the definition of the charge, which now necessarily depends on q^2. This procedure is shown in Figure 10.11, where the infinite sum over the self-energy corrections to the photon with bare charge e_0, indicated by the blob, is replaced by a $1/q^2$ propagator with effective charge $e(q^2)$.

The effective photon propagator, here denoted as P, can be expressed in terms of the propagator with the bare charge,

$$\boxed{P_0 = \frac{e_0^2}{q^2},}$$

by inserting an infinite series of the fermion loops. Each loop introduces a correction factor $\pi(q^2)$, such that the effective propagator is given by

$$P = P_0 + P_0\,\pi(q^2)\,P_0 + P_0\,\pi(q^2)\,P_0\,\pi(q^2)\,P_0 + \cdots,$$

where, for example, the second term in the above sum corresponds to a single loop correction $\pi(q^2)$ inserted between two bare P_0 propagator terms, and therefore represents the second diagram in Figure 10.11. This geometric series can be summed to give

$$P = P_0 \frac{1}{1 - \pi(q^2)\, P_0} = P_0 \frac{1}{1 - e_0^2\, \Pi(q^2)},$$

where $\Pi(q^2) = \pi(q^2)/q^2$ is the one-loop photon self-energy correction. The effective propagator can then be expressed in terms of the running coupling $e(q^2)$ as

$$P \equiv \frac{e^2(q^2)}{q^2} = \frac{e_0^2}{q^2} \frac{1}{1 - e_0^2\, \Pi(q^2)}.$$

Since scattering cross sections are known to be finite, it is an experimentally established fact that $e(q^2)$ is finite, therefore

$$e^2(q^2) = \frac{e_0^2}{1 - e_0^2\, \Pi(q^2)}, \tag{10.15}$$

is finite, even though the denominator contains $\Pi(q^2)$ which is divergent. If the physical electron charge is known at some scale $q^2 = \mu^2$, then (10.15) can be rearranged to give an expression for the bare charge

$$e_0^2 = \frac{e^2(\mu^2)}{1 + e^2(\mu^2)\Pi(\mu^2)},$$

which can be substituted back into (10.15) to give the exact relation,

$$e^2(q^2) = \frac{e^2(\mu^2)}{1 - e^2(\mu^2) \cdot [\Pi(q^2) - \Pi(\mu^2)]}. \tag{10.16}$$

As a result of the loop integral for the photon self-energy, both $\Pi(q^2)$ and $\Pi(\mu^2)$ are separately divergent. However, the difference $\Pi(q^2) - \Pi(\mu^2)$ is finite and calculable. Although the infinities have been renormalised away, the finite difference between the effective strength of the interaction at different values of q^2 remains. Consequently, the coupling strength is no longer constant, it runs with the q^2 scale of the virtual photon. For values of q^2 and μ^2 larger than the electron mass squared, it can be shown that

$$\Pi(q^2) - \Pi(\mu^2) \approx \frac{1}{12\pi^2} \ln\left(\frac{q^2}{\mu^2}\right).$$

Substituting this into (10.16) and writing $\alpha(q^2) = e^2(q^2)/4\pi$ gives

$$\boxed{\alpha(q^2) = \frac{\alpha(\mu^2)}{1 - \alpha(\mu^2)\frac{1}{3\pi}\ln\left(\frac{q^2}{\mu^2}\right)},} \tag{10.17}$$

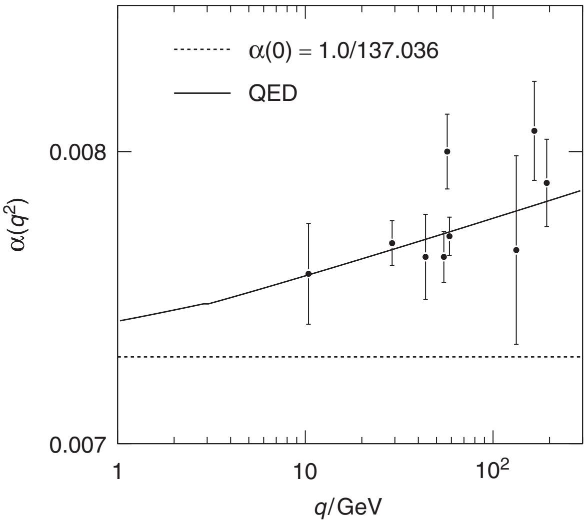

Fig. 10.12 Measurements of $\alpha(q^2)$ at different q^2 scales from $e^+e^- \to f\bar{f}$ with the OPAL experiment at LEP. The dotted line shows the low-q^2 limit of $\alpha \approx 1/137$. Adapted from Abbiendi *et al.* (2004).

and the coupling has acquired a dependence on the q^2 of the photon. Hence, the lowest-order QED diagram with a running coupling constant $\alpha(q^2)$ incorporates the effects of the virtual loop diagrams in the photon propagator. The above derivation applies equally to s-channel and t-channel processes and (10.17) holds in both cases. In a t-channel process both q^2 and μ^2 are negative and the running of the coupling constant is often written as $\alpha(Q^2)$. It should be noted that $\alpha(q^2)$ should be read as $\alpha(|q^2|)$.

The minus sign in (10.17) implies that the coupling of QED increases with increasing $|q^2|$, although the evolution is rather slow. In measurements from atomic physics at $q^2 \approx 0$, the fine-structure constant is determined to be

$$\alpha(q^2 \approx 0) = \frac{1}{137.035\,999\,074(94)}.$$

The QED coupling $\alpha(q^2)$ has also been measured in e^+e^- annihilation at LEP; the results from the highest q^2 measurements are shown in Figure 10.12. At a mean centre-of-mass energy of $\sqrt{s} = 193\,\text{GeV}$, it is found that

$$\alpha = \frac{1}{127.4 \pm 2.1},$$

providing a clear demonstration of the running of the coupling of QED.

10.5.2 Running of α_S

The treatment of renormalisation in QCD is similar to that of QED. However, owing to the gluon–gluon self-interactions, there are additional loop diagrams, as

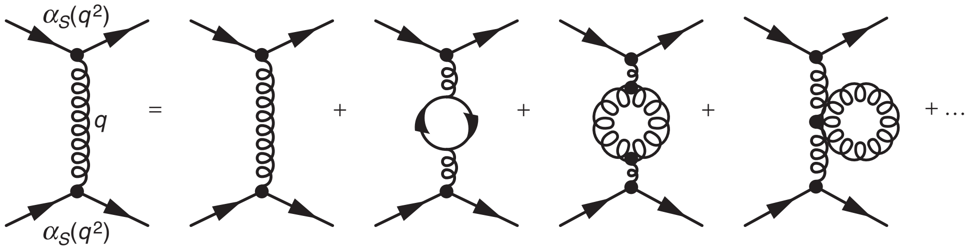

Fig. 10.13 Renormalisation in QCD.

shown in Figure 10.13. For values of q^2 and μ^2 larger than the confinement scale, the difference between the gluon self-energy again grows logarithmically

$$\Pi_S(q^2) - \Pi_S(\mu^2) \approx -\frac{B}{4\pi}\ln\left(\frac{q^2}{\mu^2}\right),$$

where the B depends to the numbers of fermionic (quark) and bosonic (gluon) loops. For N_f quark flavours and N_c colours,

$$B = \frac{11N_c - 2N_f}{12\pi}.$$

The effect of the bosonic loops enters the expression for the q^2 evolution of α_S with the opposite sign to the pure fermion loops, with the fermion loops leading to a negative contributions (which was also the case for QED) and the gluon loops leading to positive contributions. The corresponding evolution of $\alpha_S(q^2)$ is

$$\alpha_S(q^2) = \frac{\alpha_S(\mu^2)}{1 + B\,\alpha_S(\mu^2)\ln\left(\frac{q^2}{\mu^2}\right)}.$$

For $N_c = 3$ colours and $N_f \leq 6$ quarks, B is greater than zero and hence α_S *decreases* with increasing q^2.

There are many ways in which α_S can be measured. These include studies of the hadronic decays of the tau-lepton, the observed spectra of bound states of heavy quarks ($c\bar{c}$ and $b\bar{b}$), measurements of deep inelastic scattering, and jet production rates in e^+e^- annihilation. Figure 10.14 shows a summary of the most precise measurements of α_S which span $|q| = 2 - 200$ GeV. The predicted decrease in α_S with increasing $|q|$ is clearly observed and the data are consistent with the QCD predictions for the running of α_S with a value of α_S at $|q^2| = m_Z^2$ of

$$\alpha_S(m_Z^2) = 0.1184 \pm 0.0007.$$

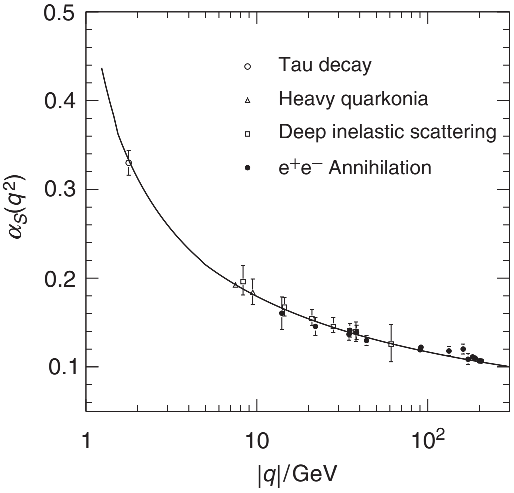

Fig. 10.14 Measurements of α_S at different $|q|$ scales. The barely noticeable kinks in the QCD prediction occur at the thresholds for producing $s\bar{s}$, $c\bar{c}$ and $b\bar{b}$; these affect the evolution of α_S as the number of effective fermion flavours N_f changes. Adapted from Bethke (2009).

Asymptotic freedom

The strength of the QCD coupling varies considerably over the range of energies relevant to particle physics. At $|q| \sim 1\,\text{GeV}$, α_S is of $\mathcal{O}(1)$ and perturbation theory cannot be used. This non-perturbative regime applies to the discussion of bound hadronic states and the latter stages in the hadronisation process. At $|q| > 100\,\text{GeV}$, which is the typical scale for modern high-energy collider experiments, $\alpha_S \sim 0.1$, which is sufficiently small that perturbation theory again can be used. This property of QCD is known as *asymptotic freedom*. It is the reason that, in the previous discussion of deep inelastic scattering at high q^2, the quarks could be treated as quasi-free particles, rather than being strongly bound within the proton. It should be noted that at high q^2, even though $\alpha_S \sim 0.1$ is sufficiently small for perturbation theory to be applicable, unlike QED, it is not so small that higher-order corrections can be neglected. For this reason, QCD calculations for processes at the LHC are almost always calculated beyond lowest order. These calculations, which often involve many Feynman diagrams, are extremely challenging.

10.6 QCD in electron–positron annihilation

A number of the properties of QCD can be studied at an electron–positron collider, primarily through the production of $q\bar{q}$ pairs in the annihilation process $e^+e^- \to q\bar{q}$, shown Figure 10.15. There are a number of advantages in studying QCD at an electron–positron collider compared to at a hadron collider. The QED production

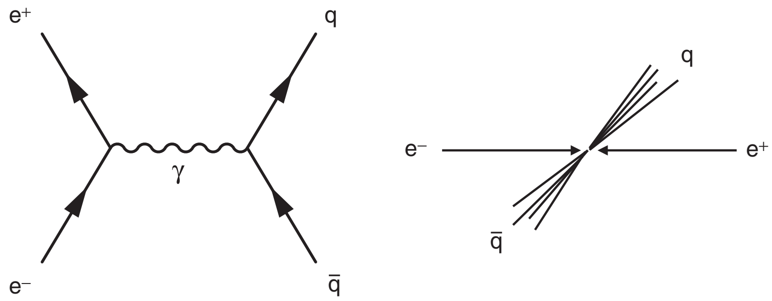

Fig. 10.15 The lowest-order QED Feynman diagram for $e^+e^- \to q\bar{q}$ production and the appearance of the interaction in a detector as a final state consisting of two jets of hadrons.

process of e^+e^- annihilation is well understood and can be calculated to high precision; there are no uncertainties related to the parton distribution functions. In addition, the observed final state corresponds to the underlying hard interaction. This is not the case for hadron–hadron collisions, where the remnants of the colliding hadrons are also observed, typically as forward-going jets.

The differential cross-section for the process $e^+e^- \to \mu^+\mu^-$ was calculated in Chapter 6. Assuming that quarks are spin-half particles, the angular dependence of the differential cross section for $e^+e^- \to q\bar{q}$ is expected to be

$$\frac{d\sigma}{d\Omega} \propto (1 + \cos^2\theta),$$

where θ is the angle between the incoming e^- and the final-state quark. Because the quark and antiquark will hadronise into jets of hadrons, it is not generally possible to identify experimentally which flavour of quark was produced. For this reason, the $e^+e^- \to q\bar{q}$ cross section is usually expressed as an inclusive sum over all quark flavours, $e^+e^- \to$ hadrons. Furthermore, it is also not usually possible to identify which jet came from the quark and which jet came from the antiquark. To reflect this ambiguity, the differential cross section is usually quoted in terms of $|\cos\theta|$. For example, Figure 10.16 shows the observed angular distribution of the jets in the process $e^+e^- \to$ hadrons in the centre-of-mass energy range $38.8 < \sqrt{s} < 46.5$ GeV. The angular distribution is consistent with expected $(1 + \cos^2\theta)$ form, demonstrating that quarks are indeed spin-half particles.

The total QED $e^+e^- \to \mu^+\mu^-$ cross section, was calculated previously

$$\sigma(e^+e^- \to \mu^+\mu^-) = \frac{4\pi\alpha^2}{3s}. \tag{10.18}$$

The corresponding cross section for the QED production of a $q\bar{q}$ pair is

$$\sigma(e^+e^- \to q\bar{q}) = 3 \times \frac{4\pi\alpha^2}{3s} Q_q^2, \tag{10.19}$$

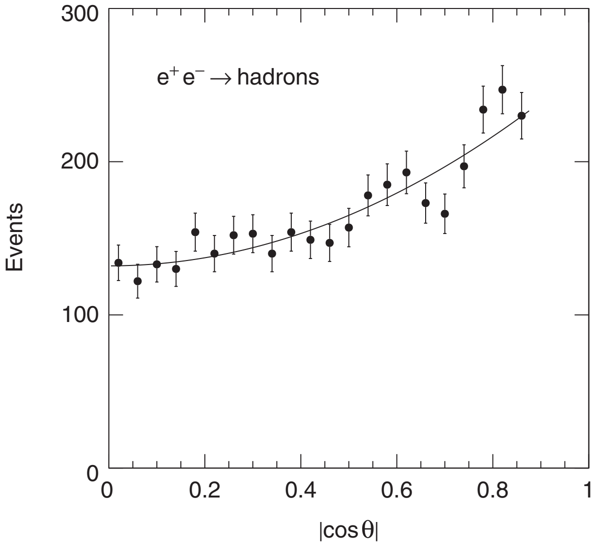

Fig. 10.16 The angular distribution of the jets produced in e^+e^- annihilation at centre-of-mass energies between 38.8 GeV $< \sqrt{s} <$ 46.5 GeV as observed in the CELLO experiment at the PETRA e^+e^- collider at DESY. The expected $(1+\cos^2\theta)$ distribution for the production of spin-half particles is also shown. Adapted from Behrend *et al.* (1987).

where the factor of three accounts for the sum over the three possible colour combinations of the final-state $q\overline{q}$ that can be produced as $g\overline{g}$, $r\overline{r}$ or $b\overline{b}$. The inclusive QED cross section for $\sigma(e^+e^- \to \text{hadrons})$ is the sum of the cross sections for the quark flavours that are kinematically accessible at a given centre-of-mass energy ($\sqrt{s} > 2m_q$),

$$\sigma(e^+e^- \to \text{hadrons}) = \frac{4\pi\alpha^2}{s} \times 3 \sum_{\text{flavours}} Q_q^2. \tag{10.20}$$

It is convenient to express the inclusive cross section of (10.20) in terms of a ratio relative to the $\mu^+\mu^-$ cross section of (10.18),

$$R_\mu \equiv \frac{\sigma(e^+e^- \to \text{hadrons})}{\sigma(e^+e^- \to \mu^+\mu^-)} = 3 \sum_{\text{flavours}} Q_q^2. \tag{10.21}$$

This has the advantage that a number of experimental systematic uncertainties cancel since R_μ is related to the ratio of the observed numbers of events. The expected value of R_μ depends on the sum of the squares of the charges of the quark flavours that can be produced at a particular centre-of-mass energy. For $\sqrt{s} \lesssim 3\,\text{GeV}$, only u, d and s quarks can be produced, giving the predicted value

$$R_\mu^{\text{d,u,s}} = 3 \times \left(\tfrac{4}{9} + \tfrac{1}{9} + \tfrac{1}{9}\right) = 2.$$

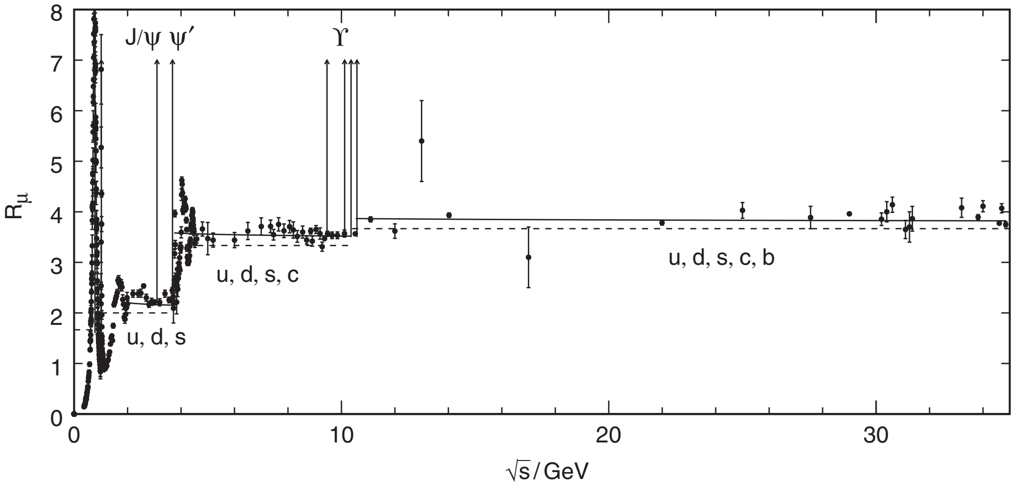

Fig. 10.17 Experimental measurements of R_μ as a function of $\sqrt{s}$. The dashed line is the lowest-order prediction assuming three colours. The solid line includes the first-order QCD correction of $(1 + \alpha_S(q^2)/\pi)$. Based on data compiled by the Particle Data Group, Beringer *et al.* (2012).

Above the thresholds for $\mathrm{c\overline{c}}$ production (3.1 GeV) and $\mathrm{b\overline{b}}$ production (9.5 GeV) the predictions for R_μ are respectively

$$R_\mu^{\mathrm{c}} = 3\times\left(\tfrac{1}{9}+\tfrac{4}{9}+\tfrac{1}{9}+\tfrac{4}{9}\right)=\tfrac{10}{3} \quad \text{and} \quad R_\mu^{\mathrm{b}} = 3\times\left(\tfrac{1}{9}+\tfrac{4}{9}+\tfrac{1}{9}+\tfrac{4}{9}+\tfrac{1}{9}\right)=\tfrac{11}{3}.$$

Figure 10.17 shows the measurements of R_μ over a wide range of centre-of-mass energies. At relatively low energies, there is significant structure due to resonant production of bound $\mathrm{q\overline{q}}$ states with the same spin and parity as the virtual photon, $J^P = 1^-$. These resonances greatly enhance the $\mathrm{e^+e^-} \to$ hadrons cross section when the centre-of-mass energy is close to the mass of the state being produced. At very low energies, the resonance structure is dominated by the $J^P = 1^-$ mesons introduced in Section 9.6.3, namely the ρ^0(770 MeV), ω(782 MeV) and ϕ(1020 MeV) mesons. At higher energies, charmonium ($\mathrm{c\overline{c}}$) and bottomonium ($\mathrm{b\overline{b}}$) states are produced, such as the J/ψ(3097 MeV), ψ'(3686 MeV) and Υ states. These heavy quark resonances are discussed further in Section 10.8.

In the continuum between the meson resonances, the data disagree with the predictions for R_μ given in (10.21) at the level of approximately 10%. The origin of the discrepancy is that the cross sections of (10.18) and (10.19) are only relevant for the lowest-order process, whereas the measured cross sections will include $\mu^+\mu^-\gamma$, $\mathrm{q\overline{q}}\gamma$ and $\mathrm{q\overline{q}g}$ final states, as shown in Figure 10.18. The cross sections for these processes will be suppressed relative to the lowest-order process by respective factors of α, α and α_S due to the additional vertex. The QED corrections are relatively

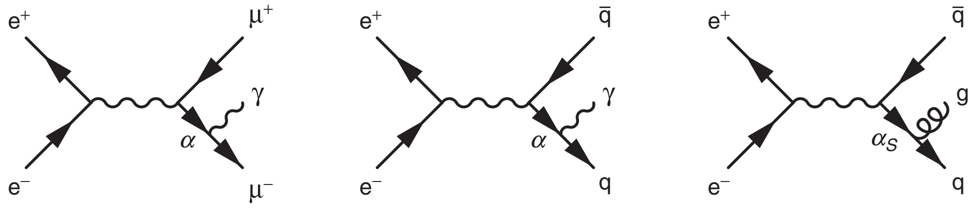

Fig. 10.18 Feynman diagrams for $e^+e^- \to \mu^+\mu^-\gamma, q\bar{q}\gamma, q\bar{q}g$.

small, but the $O(\alpha_S)$ correction cannot be neglected. If the first-order QCD correction from $e^+e^- \to q\bar{q}g$ is included, the prediction of (10.21) is modified to

$$R_\mu = \frac{\sigma(e^+e^- \to \text{hadrons})}{\sigma(e^+e^- \to \mu^+\mu^-)} = 3\left(1 + \frac{\alpha_S(q^2)}{\pi}\right) \sum_{\text{flavours}} Q_q^2. \tag{10.22}$$

With the QCD correction included, the prediction for R_μ, shown by the solid line in Figure 10.17, is in excellent agreement with the experimental measurements away from the resonances. This agreement provides strong evidence for the existence of colour (which is never directly observed); without the additional colour degree of freedom, the prediction for R_μ would be a factor of three smaller and would be incompatible with the observed data.

Gluon production in e^+e^- annihilation

Jet production in high-energy electron–positron collisions also provides direct evidence for the existence of gluons. Figure 10.19 shows three examples of $e^+e^- \to$ hadrons events observed in the OPAL detector at LEP. Whilst the majority of the $e^+e^- \to$ hadrons events are produced with a clear two-jet topology, final states with three- or four-jets are also observed. The three-jet events originate from the process $e^+e^- \to q\bar{q}g$, where the gluon is radiated from either the final-state quark or antiquark, as shown in Figure 10.19b. The relative cross section for the production of three-jet events compared to the two-jet final states is proportional to α_S. Hence the observed number of three-jet events relative to the number of two-jet events, provides one of the most precise measurements of $\alpha_S(q^2)$. Jet production in electron–positron collisions also provides a direct test of the SU(3) group structure of QCD. For example, one of the Feynman diagrams for four-jet production, shown in Figure 10.19c, involves the triple gluon vertex. The Feynman rules for this vertex are determined by the local gauge symmetry of QCD. By studying the angular distributions of the jets in four-jet events, it is possible to distinguish between an underlying SU(3) colour symmetry and alternative gauge symmetries. Needless to say, the experimental data are consistent with the predictions of SU(3).

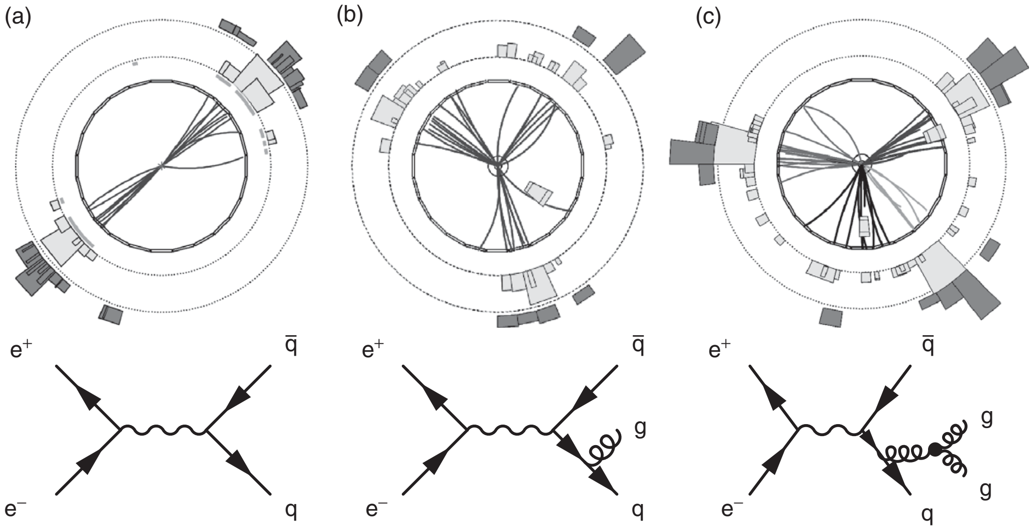

Fig. 10.19 Jet production in e^+e^- annihilation. The example events were recorded at $\sqrt{s} = 91$ GeV by the OPAL experiment at LEP in the mid 1990s. They correspond to (a) $e^+e^- \rightarrow q\bar{q} \rightarrow$ two-jets, (b) $e^+e^- \rightarrow q\bar{q}g \rightarrow$ three-jets and (c) $e^+e^- \rightarrow q\bar{q}gg \rightarrow$ four-jets. Reproduced courtesy of the OPAL collaboration. Also shown are possible Feynman diagrams corresponding to the observed events. In the case of four-jet production there are also diagrams where both gluons are radiated from the quarks.

10.7 Colour factors

At hadron colliders, such as the LHC, the observed event rates are dominated by the QCD scattering of quarks and gluons. Figure 10.20 shows one of the parton-level processes contributing to the cross section for pp → two jets + X, where X represents the remnants of the proton that are observed as forward jets in the direction of the incoming proton beams. The calculation of the corresponding matrix element needs to account for the different colours of the quarks and gluons that can contribute to the scattering process.

In the Feynman diagram of Figure 10.20, the incoming and outgoing quark colours are labelled by i, j, k and l. The exchanged gluon is labelled by a and b at the two vertices, with the δ^{ab} term in the propagator ensuring that the gluon at vertex μ is the same as that at vertex ν. The colour flow in the diagram corresponds to $ik \rightarrow jl$. There are 3^4 possible colour combinations for the four quarks involved in this process. In addition, there and eight possible gluons that can be exchanged. Consequently, there are 648 distinct combinations of quark colours and gluons that potentially can contribute to the process. Fortunately, the effect of summing over all the colour and gluon combinations can be absorbed into a single *colour factor*.

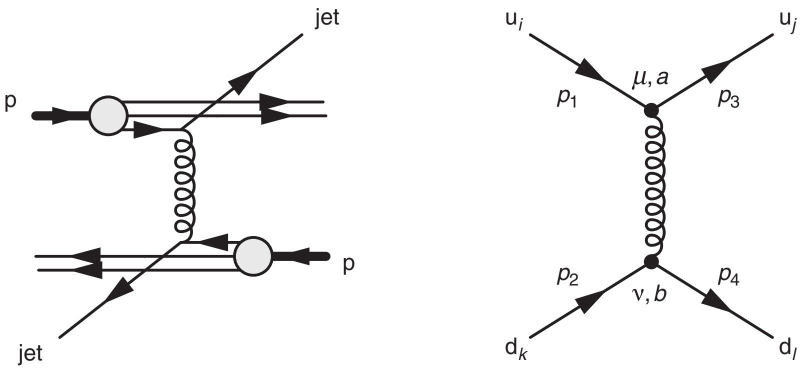

Fig. 10.20 One of the processes contributing to two-jet production in pp collisions at the LHC, shown in terms of the colliding protons and one of the contributing Feynman diagram, with quark colours $ik \to jl$.

The matrix element for the Feynman diagram of Figure 10.20 can be written down using the Feynman rules for QCD:

$$-i\mathcal{M} = \left[\overline{u}(p_3)\{-\tfrac{1}{2}ig_S\lambda^a_{ji}\gamma^\mu\}u(p_1)\right]\frac{-ig_{\mu\nu}}{q^2}\delta^{ab}\left[\overline{u}(p_4)\{-\tfrac{1}{2}ig_S\lambda^b_{lk}\gamma^\nu\}u(p_2)\right].$$

This can be rearranged to give

$$\mathcal{M} = -\frac{g_S^2}{4}\lambda^a_{ji}\lambda^a_{lk}\frac{1}{q^2}g_{\mu\nu}[\overline{u}(p_3)\gamma^\mu u(p_1)][\overline{u}(p_4)\gamma^\nu u(p_2)]. \tag{10.23}$$

This matrix element resembles that for the QED process $e^-q \to e^-q$ given in (8.13),

$$\mathcal{M} = Q_q\frac{e^2}{q^2}g_{\mu\nu}[\overline{u}(p_3)\gamma^\mu u(p_1)][\overline{u}(p_4)\gamma^\nu u(p_2)].$$

The QCD matrix element for a particular combination of quark colours can be obtained from the calculated QED matrix element by making the replacements $-Q_q e^2 \to g_S^2$, or equivalently $-Q_q\alpha \to \alpha_S$, and multiplying by the colour factor $C(ik \to jl)$ that accounts for the sum over the eight possible exchanged gluons

$$C(ik \to jl) \equiv \frac{1}{4}\sum_{a=1}^{8}\lambda^a_{ji}\lambda^a_{lk}. \tag{10.24}$$

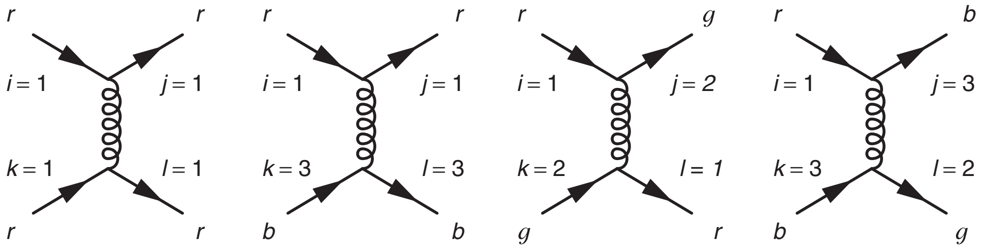

Fig. 10.21 Examples of the four classes of colour exchange diagram in quark–quark scattering.

The QCD colour factor $C(ik \to jl)$ can be evaluated using the Gell-Mann matrices

$$\lambda_1 = \begin{pmatrix} 0 & 1 & 0 \\ 1 & 0 & 0 \\ 0 & 0 & 0 \end{pmatrix}, \quad \lambda_4 = \begin{pmatrix} 0 & 0 & 1 \\ 0 & 0 & 0 \\ 1 & 0 & 0 \end{pmatrix}, \quad \lambda_6 = \begin{pmatrix} 0 & 0 & 0 \\ 0 & 0 & 1 \\ 0 & 1 & 0 \end{pmatrix}, \quad \lambda_3 = \begin{pmatrix} 1 & 0 & 0 \\ 0 & -1 & 0 \\ 0 & 0 & 0 \end{pmatrix},$$

$$\lambda_2 = \begin{pmatrix} 0 & -i & 0 \\ i & 0 & 0 \\ 0 & 0 & 0 \end{pmatrix}, \quad \lambda_5 = \begin{pmatrix} 0 & 0 & -i \\ 0 & 0 & 0 \\ i & 0 & 0 \end{pmatrix}, \quad \lambda_7 = \begin{pmatrix} 0 & 0 & 0 \\ 0 & 0 & -i \\ 0 & i & 0 \end{pmatrix}, \quad \lambda_8 = \frac{1}{\sqrt{3}}\begin{pmatrix} 1 & 0 & 0 \\ 0 & 1 & 0 \\ 0 & 0 & -2 \end{pmatrix},$$

where λ_1 and λ_2 correspond to the exchange of $r\bar{g}$ and $g\bar{r}$ gluons, λ_4 and λ_5 represent $r\bar{b}$ and $b\bar{r}$ gluons, λ_6 and λ_7 represent $g\bar{b}$ and $b\bar{g}$ gluons, and λ_3 and λ_8 represent the exchange of $\frac{1}{2}(r\bar{r} - g\bar{g})$ and $\frac{1}{\sqrt{6}}(r\bar{r} + g\bar{g} - 2b\bar{b})$ gluons. The 3^4 possible combinations of the colours i, j, k and l can be categorised into the four classes of colour exchange, shown in Figure 10.21. These correspond to the following cases: all four colours are the same, e.g. $rr \to rr$; the two initial-state quarks have different colours but do not change colour, e.g. $rb \to rb$; the two initial-state quarks have different colours and exchange colour, e.g. $rb \to br$; and all three colours are involved. The different colour indices determine which elements of the λ-matrices are relevant to the scattering process, which in turn determines which gluons contribute.

From (10.24) the colour factor for $rr \to rr$ is

$$C(rr \to rr) \equiv \frac{1}{4}\sum_{a=1}^{8} \lambda^a_{11}\lambda^a_{11}.$$

Here the non-zero contributions arise from λ_3 and λ_8, which are the only Gell-Mann matrices with non-zero values in the 11-element. Hence

$$\begin{aligned} C(rr \to rr) &= \frac{1}{4}\sum_{a=1}^{8} \lambda^a_{11}\lambda^a_{11} = \frac{1}{4}(\lambda^3_{11}\lambda^3_{11} + \lambda^8_{11}\lambda^8_{11}) \\ &= \frac{1}{4}\left(1 + \tfrac{1}{3}\right) = \tfrac{1}{3}. \end{aligned}$$

Because of the underlying exact SU(3) colour symmetry, there is no need to repeat the exercise for $gg \to gg$ or $bb \to bb$; the SU(3) colour symmetry guarantees that the same result will be obtained, thus

$$\boxed{C(rr \to rr) = C(gg \to gg) = C(bb \to bb) = \tfrac{1}{3}.} \tag{10.25}$$

For the second class of diagram of Figure 10.21, $rb \to rb$, the corresponding colour factor is

$$C(rb \to rb) = \frac{1}{4}\sum_{a=1}^{8} \lambda^a_{11}\lambda^a_{33}.$$

Hence only the gluons associated with the Gell-Mann matrices with non-zero entries in the 11 *and* 33 positions give a non-zero contribution, thus

$$C(rb \to rb) = \frac{1}{4}\sum_{a=1}^{8} \lambda^a_{11}\lambda^a_{33} = \frac{1}{4}\lambda^8_{11}\lambda^8_{33} = \frac{1}{4}\left(\tfrac{1}{\sqrt{3}} \cdot \tfrac{-2}{\sqrt{3}}\right) = -\frac{1}{6},$$

and, from the SU(3) colour symmetry,

$$\boxed{\begin{aligned} &C(rb \to rb) = C(rg \to rg) = C(gr \to gr) = \\ &C(gb \to gb) = C(br \to br) = C(bg \to bg) = -\tfrac{1}{6}. \end{aligned}} \tag{10.26}$$

For the third class of colour exchange of Figure 10.21, $rg \to gr$, the only non-zero contributions arise from the λ-matrices with non-zero entries in the 12 *and* 21 positions, therefore

$$C(rg \to gr) = \frac{1}{4}\sum_{a=1}^{8} \lambda^a_{21}\lambda^a_{12} = \frac{1}{4}\left(\lambda^1_{21}\lambda^1_{12} + \lambda^2_{21}\lambda^2_{12}\right) = \frac{1}{2},$$

and thus

$$\boxed{\begin{aligned} &C(rb \to br) = C(rg \to gr) = C(gr \to rg) = \\ &C(gb \to bg) = C(br \to rb) = C(bg \to gb) = \tfrac{1}{2}. \end{aligned}} \tag{10.27}$$

Finally, for the case where three different colours are involved, e.g. $rb \to bg$,

$$C(rb \to bg) = \frac{1}{4}\sum_{a=1}^{8} \lambda^a_{31}\lambda^a_{23}.$$

Because none of the λ-matrices has non-zero entries in both the 31 and 23 positions, the colour factor is zero. This should come as no surprise, colour is a conserved charge of the SU(3) colour symmetry and the process $rb \to bg$ would result in a net change of colour.

Averaged colour factor

The colour factors calculated above account for the summation over the eight possible gluon intermediate states for a particular colour exchange $ik \to jl$. In the scattering process ud → ud, the colours of each of the initial-state quarks are equally likely to be r, b or g. Therefore the nine possible initial-state colour combinations are equally probable. For a particular initial-state colour combination, the cross section will depend on the sum of the squared matrix elements for each of the nine possible orthogonal final-state colour combinations. The possible colour combinations are accounted for by the colour-averaged sum of squared matrix elements,

$$\langle|\mathcal{M}|^2\rangle = \frac{1}{9}\sum_{i,j,k,l=1}^{3}|\mathcal{M}(ij\to kl)|^2, \tag{10.28}$$

where the sum is over all possible colours in the initial- and final-state, and the factor of $\frac{1}{9}$ averages over the nine possible initial-state colour combinations. The colour part of (10.28),

$$\langle|C|^2\rangle = \frac{1}{9}\sum_{i,j,k,l=1}^{3}|C(ij\to kl)|^2, \tag{10.29}$$

can be evaluated using the expressions for the individual colour factors of (10.25)–(10.27). There are three colour combinations of the type $rr \to rr$ (i.e. $rr \to rr$, $bb \to bb$ and $gg \to gg$) each with an individual colour factor $\frac{1}{3}$, six combinations of the type $rb \to rb$ with colour factor $-\frac{1}{6}$ and six combinations of the type $rb \to br$ with colour factor $\frac{1}{2}$. Hence the overall colour factor is

$$\langle|C|^2\rangle = \tfrac{1}{9}\left[3\times\left(\tfrac{1}{3}\right)^2 + 6\times\left(-\tfrac{1}{6}\right)^2 + 6\times\left(\tfrac{1}{2}\right)^2\right] = \tfrac{2}{9}. \tag{10.30}$$

Hence, the entire effect of the 648 possible combinations of quark colours and types of gluons is encompassed into a single number.

The QCD cross section for the scattering process ud → ud can be obtained from the QED cross section for $e^-q \to e^-q$ of (8.19),

$$\frac{d\sigma}{dq^2} = \frac{2\pi Q_q^2\alpha^2}{q^4}\left[1+\left(1+\frac{q^2}{s}\right)^2\right],$$

by replacing αQ_q with α_S and by multiplying by the averaged colour factor of (10.30), to give

$$\frac{d\sigma}{dq^2} = \frac{4\pi\alpha_S^2}{9q^4}\left[1+\left(1+\frac{q^2}{\hat{s}}\right)^2\right], \tag{10.31}$$

where $\hat{s}$ is the centre-of-mass energy of the colliding ud system.

10.7.1 Colour in processes with antiquarks

Figure 10.22 shows the vertices for the basic QCD interaction between quarks and/or antiquarks. The quark current associated with the qqg vertex is given by (10.12)

$$j_{\mathrm{q}}^{\mu} = \overline{u}(p_3)c_j^{\dagger}\left\{-\tfrac{1}{2}ig_S\lambda^a\gamma^{\mu}\right\}c_i u(p_1),$$

where the outgoing quark enters as the adjoint spinor. In the equivalent expression for the $\overline{\mathrm{q}}\,\overline{\mathrm{q}}$g vertex, the incoming antiparticle is now represented by the adjoint spinor

$$j_{\overline{\mathrm{q}}}^{\mu} = \overline{v}(p_1)c_i^{\dagger}\left\{-\tfrac{1}{2}ig_S\lambda^a\gamma^{\mu}\right\}c_j v(p_3).$$

Consequently, the colour part of the expression is

$$c_i^{\dagger}\lambda^a c_j = c_i^{\dagger}\begin{pmatrix}\lambda^a_{1j}\\ \lambda^a_{2j}\\ \lambda^a_{3j}\end{pmatrix} = \lambda^a_{ij}.$$

The order of the indices ij is swapped with respect to the quark case, $ji \to ij$. In general, the colour index associated with the adjoint spinor appears first, and thus the colour factor associated with the q$\overline{\mathrm{q}}$g annihilation vertex shown of Figure 10.22 is λ^a_{ki}.

Figure 10.23 shows the four possible combinations of two quarks/antiquarks interacting via the exchange of a single gluon. For the quark–antiquark and antiquark–antiquark scattering diagrams, the expressions for the colour factors are

$$C(\overline{i}\,\overline{k} \to \overline{j}\,\overline{l}) \equiv \frac{1}{4}\sum_{a=1}^{8}\lambda^a_{ij}\lambda^a_{kl}, \quad \text{and} \quad C(i\overline{k} \to j\overline{l}) \equiv \frac{1}{4}\sum_{a=1}^{8}\lambda^a_{ji}\lambda^a_{kl},$$

which can be compared to the expression for the colour factor for quark–quark scattering of (10.24). Because the Gell-Mann matrices have the property that either $\lambda^{\mathrm{T}} = \lambda$ or $\lambda^{\mathrm{T}} = -\lambda$, the same colour factors are obtained for qq and $\overline{\mathrm{q}}\,\overline{\mathrm{q}}$ scattering,

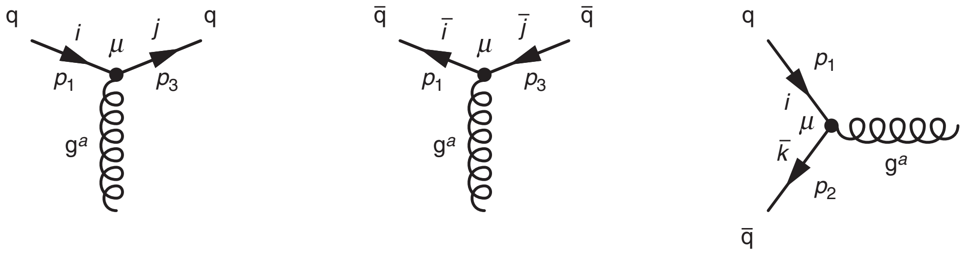

Fig. 10.22 Colour indices for the qqg, $\overline{\mathrm{q}}\overline{\mathrm{q}}$g and q$\overline{\mathrm{q}}$g vertices.

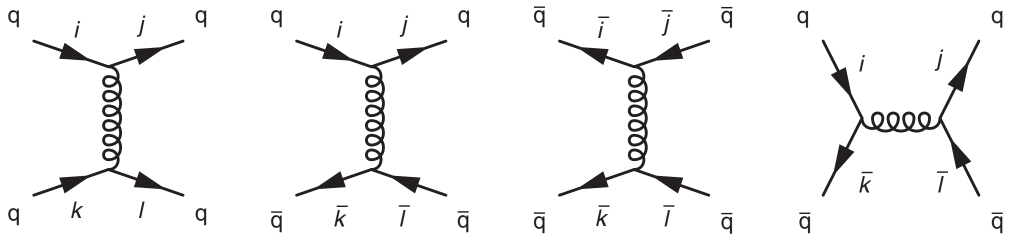

Fig. 10.23 The four diagrams involving the interaction of two quarks/antiquarks via a single gluon.

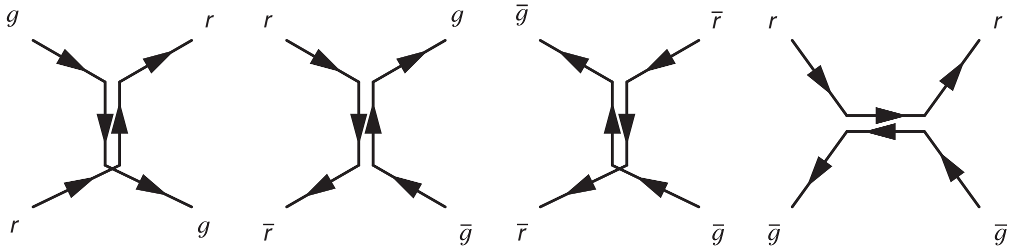

Fig. 10.24 Examples of colour flow in the t-channel scattering processes of ud $\rightarrow$ ud, u$\overline{\text{d}}$ $\rightarrow$ u$\overline{\text{d}}$ and $\overline{\text{u}}\overline{\text{d}}$ $\rightarrow$ $\overline{\text{u}}\overline{\text{d}}$ scattering, and the s-channel annihilation process q$\overline{\text{q}}$ $\rightarrow$ q$\overline{\text{q}}$. In each case the gluons exchanged are $r\overline{g}$ and $g\overline{r}$.

and it is straightforward to show that the non-zero colour factors for the t-channel scattering processes are

$$C(r\,r \to r\,r) = C(r\,\overline{r} \to r\,\overline{r}) = C(\overline{r}\,\overline{r} \to \overline{r}\,\overline{r}) = \tfrac{1}{3}, \tag{10.32}$$

$$C(r\,g \to r\,g) = C(r\,\overline{g} \to r\,\overline{g}) = C(\overline{r}\,\overline{g} \to \overline{r}\,\overline{g}) = -\tfrac{1}{6}, \tag{10.33}$$

$$C(r\,g \to g\,r) = C(r\,\overline{r} \to g\,\overline{g}) = C(\overline{r}\,\overline{g} \to \overline{g}\,\overline{r}) = \tfrac{1}{2}. \tag{10.34}$$

For the s-channel annihilation diagram, the expression for the individual colour factors is

$$C_s(i\,\overline{k} \to j\overline{l}) \equiv \frac{1}{4}\sum_{a=1}^{8} \lambda^a_{ki}\lambda^a_{jl},$$

from which it follows that

$$C_s(r\,\overline{r} \to r\,\overline{r}) = \tfrac{1}{3}, \quad C_s(r\,\overline{g} \to r\,\overline{g}) = \tfrac{1}{2} \quad \text{and} \quad C_s(r\,\overline{r} \to g\,\overline{g}) = -\tfrac{1}{6}. \tag{10.35}$$

For all four processes shown in Figure 10.23, the colour-averaged colour factor, defined in (10.29), is $\langle |C|^2 \rangle = 2/9$. Each of the individual colour factors given in (10.32)–(10.35) can be associated with the exchange of a particular type of gluon, such that colour charge is conserved at each vertex. For example, Figure 10.24 shows the colour flow in the Feynman diagrams of Figure 10.23 for the case where the virtual gluon corresponds to the combined effect of the exchange of $r\overline{g}$ and $g\overline{r}$ gluons.

10.7.2 *Colour sums revisited

The overall colour factor for quark (or antiquark) scattering via the exchange of a single gluon can be obtained directly by considering the factors that enter the expression for the matrix element squared. For example, the qq → qq matrix element $\mathcal{M}$ for colours $ik \to jl$ includes the colour factor

$$C = \frac{1}{4}\lambda^a_{ji}\lambda^a_{lk},$$

where summation over the repeated gluon indices is implied. The matrix element squared for this colour combination, $|\mathcal{M}|^2 = \mathcal{M}\mathcal{M}^\dagger$, is proportional to

$$\begin{aligned} CC^* &= \frac{1}{16}\lambda^a_{ji}\lambda^a_{lk}\cdot(\lambda^b_{ji})^*(\lambda^b_{lk})^* \\ &= \frac{1}{16}\lambda^a_{ji}\lambda^a_{lk}\lambda^b_{ij}\lambda^b_{kl}, \end{aligned} \tag{10.36}$$

where the second line follows from the Gell-Mann matrices being Hermitian. The colour-averaged summed matrix element squared therefore can be written

$$\begin{aligned} \langle |C|^2\rangle = \langle CC^*\rangle &= \frac{1}{9}\frac{1}{16}\sum_{a,b=1}^{8}\sum_{ijkl=1}^{3}\lambda^a_{ji}\lambda^b_{ij}\lambda^a_{lk}\lambda^b_{kl} \\ &= \frac{1}{144}\sum_{a,b=1}^{8}\left[\mathrm{Tr}\left(\lambda^a\lambda^b\right)\right]^2. \end{aligned}$$

It is straightforward to show that $\mathrm{Tr}\left(\lambda^a\lambda^b\right) = 2\delta_{ab}$, and thus

$$\langle |C|^2\rangle = \frac{1}{144}\sum_{a,b=1}^{8}(2\delta_{ab})^2 = \frac{1}{144}\sum_{a=1}^{8}2^2 = \frac{2}{9}.$$

The same result will be obtained independent of the order in which the indices appear in the initial expression, and therefore the same colour-averaged colour factor is obtained for all four processes of Figure 10.23.

10.8 Heavy mesons and the QCD colour potential

Heavy quark $c\bar{c}$ (charmonium) and $b\bar{b}$ (bottomonium) bound states are observed as resonances in e^+e^- annihilation, as seen previously in Figure 10.17. The multiple charmonium and bottomonium resonances correspond to eigenstates of the $q\bar{q}$ system in the QCD potential. Whilst only states with spin-parity $J^P = 1^-$ are produced in e^+e^- annihilation, other states are observed in particle decays. Unlike the quarks

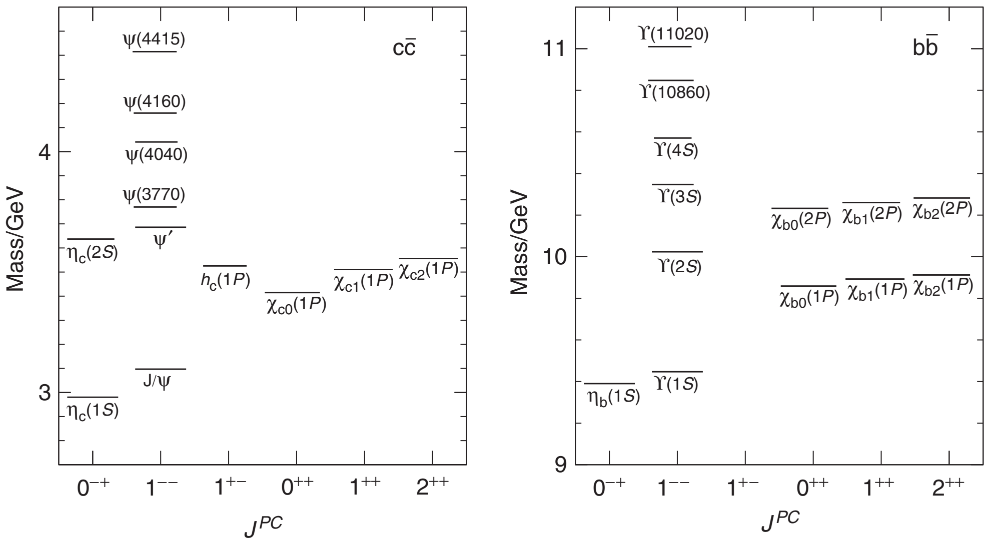

Fig. 10.25 The masses and J^{PC} assignments of the observed charmonium ($c\bar{c}$) and bottomonium ($b\bar{b}$) bound states, where C is the charge conjugation quantum number discussed in Chapter 14.

in the light uds mesons, which are relativistic, the velocities of the heavy quarks in the charmonium and bottomonium states are relatively low, $\beta_c \sim 0.3$ and $\beta_b \sim 0.1$. In this case, the observed spectra of charmonium and bottomonium states, shown in Figure 10.25, provide a probe of the QCD potential in the non-relativistic limit.

In non-relativistic QCD (NRQCD), the interaction between two quarks (or between a quark and an antiquark) can be expressed as a static potential of the form $V(\mathbf{r})$. Owing to the gluon self-interactions (10.13), the potential at large distances is proportional to the separation of the quarks, $V(\mathbf{r}) \sim \kappa \mathrm{r}$. The short-range component of the NRQCD potential can be obtained by considering the analogous situation for QED. The non-relativistic limit of QED gives rise to a repulsive Coulomb potential between two electrons (i.e. two particles), $V(\mathbf{r}) = \alpha/\mathrm{r}$, and an attractive potential between an electron and its antiparticle, $V(\mathbf{r}) = -\alpha/\mathrm{r}$. With the exception of the treatment of colour, which factorises from the spinor part, the fundamental QCD interaction has exactly the same $\overline{\phi}\gamma^{\mu}\psi$ form as QED. Therefore, the short-range NRQCD potential between two quarks must be

$$V_{\mathrm{qq}}(\mathbf{r}) = +C\frac{\alpha_S}{\mathrm{r}}, \tag{10.37}$$

and that between a quark and an antiquark is

$$V_{\mathrm{q\bar{q}}}(\mathbf{r}) = -C\frac{\alpha_S}{\mathrm{r}}, \tag{10.38}$$

where C is the appropriate colour factor. Depending on the sign of this colour factor, which will depend on the colour wavefunction of the state, the short-range static potential for the $\mathrm{q\bar{q}}$ system could be either attractive or repulsive.

From the colour confinement hypothesis, it is known that mesons are colour singlets, with a colour wavefunction

$$\psi = \frac{1}{\sqrt{3}}(r\bar{r} + g\bar{g} + b\bar{b}).$$

Thus, the expectation value of the NRQCD potential for a meson can be written

$$\langle V_{\mathrm{q}\bar{\mathrm{q}}}\rangle = \langle\psi|V_{\mathrm{QCD}}|\psi\rangle = \tfrac{1}{3}\left(\langle r\bar{r}|V_{\mathrm{QCD}}|r\bar{r}\rangle + \cdots + \langle r\bar{r}|V_{\mathrm{QCD}}|b\bar{b}\rangle + \cdots\right), \tag{10.39}$$

where the dots indicate the other seven colour combinations. From the form of the NRQCD potential identified in (10.38),

$$\langle r\bar{r}|V_{\mathrm{QCD}}|r\bar{r}\rangle = -C(r\bar{r} \to r\bar{r})\frac{\alpha_S}{\mathrm{r}} \quad \text{and} \quad \langle r\bar{r}|V_{\mathrm{QCD}}|b\bar{b}\rangle = -C(r\bar{r} \to b\bar{b})\frac{\alpha_S}{\mathrm{r}},$$

and therefore the expectation value of the QCD potential of (10.39) can be written

$$\langle V_{\mathrm{q}\bar{\mathrm{q}}}\rangle = -\frac{\alpha_S}{3\mathrm{r}}\left(C(r\bar{r} \to r\bar{r}) + \cdots + C(r\bar{r} \to b\bar{b}) + \cdots\right).$$

This expression contains three terms of the form $r\bar{r} \to r\bar{r}$ and six of the form $r\bar{r} \to g\bar{g}$, and therefore

$$\langle V_{\mathrm{q}\bar{\mathrm{q}}}\rangle = -\frac{\alpha_S}{3\mathrm{r}}\left[3 \times C(r\bar{r} \to r\bar{r}) + 6 \times C(r\bar{r} \to g\bar{g})\right].$$

Using the expressions for the colour factors for the t-channel exchange of a gluon between a quark and an antiquark, given in (10.32) and (10.34), the non-relativistic QCD potential can be written

$$\langle V_{\mathrm{q}\bar{\mathrm{q}}}\rangle = -\frac{\alpha_S}{3\mathrm{r}}\left[3 \times \tfrac{1}{3} + 6 \times \tfrac{1}{2}\right] = -\frac{4}{3}\frac{\alpha_S}{\mathrm{r}}.$$

Hence, the short range NRQCD potential in the $\mathrm{q}\bar{\mathrm{q}}$ colour singlet state is attractive. Adding in the long-range term of (10.13), gives the expression for the NRQCD potential

$$\boxed{V_{\mathrm{q}\bar{\mathrm{q}}}(\mathbf{r}) = -\frac{4}{3}\frac{\alpha_S}{\mathrm{r}} + \kappa\mathrm{r}.} \tag{10.40}$$

The non-relativistic QCD potential of (10.40) can be used to obtain the predicted spectra for the $\mathrm{c}\bar{\mathrm{c}}$ and $\mathrm{b}\bar{\mathrm{b}}$ bound states. The more accurate predictions are obtained for the $\mathrm{b}\bar{\mathrm{b}}$ system, where the non-relativistic treatment is a good approximation. Reasonable agreement with observed $l = 0$ and $l = 1$ charmonium and bottomonium states of Figure 10.25 is found assuming $\lambda \approx 1\,\mathrm{GeV/fm}$, providing further evidence for the presence of the linear term in the potential, which is believed to be responsible for colour confinement.

Figure 10.26 shows the non-relativistic QCD potential of (10.40) for $\alpha_S = 0.2$ and $\kappa = 1\,\mathrm{GeV/fm}$. The potential energy becomes positive at approximately 0.25 fm, with the linear term dominating at larger radii, setting the length scale for confinement for these heavy quark states.

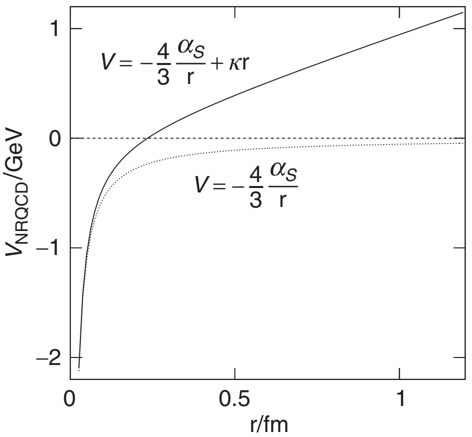

Fig. 10.26 The approximate form of the non-relativistic QCD potential for a bound $q\bar{q}$ state, assuming $\alpha_S = 0.2$ and $\kappa = 1\,\mathrm{GeV/\,fm}$.

10.9 Hadron–hadron collisions

Hadron colliders, either proton–proton or proton–antiproton, provide a route to achieving higher centre-of-mass energies than is possible with circular e^+e^- colliders, and are central to the search for the production of new particles at high-mass scales. The underlying process in hadron–hadron collisions is the interaction of two partons, which can be either quarks, antiquarks or gluons.

10.9.1 Hadron collider event kinematics

In electron–proton elastic scattering, a single variable was sufficient to describe the event kinematics. This was chosen to be the scattering angle of the electron. In electron–proton deep inelastic scattering two variables are required, reflecting the additional degree of freedom associated with the unknown momentum fraction x of the struck quark. In hadron–hadron collisions, the momentum fractions x_1 and x_2 of the two interacting partons are unknown, and the event kinematics have to be described by three variables, for example Q^2, x_1 and x_2. These three independent kinematic variables can be related to three experimentally well-measured quantities. In hadron collider experiments, the scattered partons are observed as jets. In a process such as $\mathrm{pp} \rightarrow$ two jets $+\, X$, the angles of the two-jets with respect to the beam axis are relatively well measured. Consequently, differential cross sections are usually described in terms of these two jet angles and the component of momentum of one of the jets in the plane transverse to the beam axis, referred to as the transverse momentum

$$p_T = \sqrt{p_x^2 + p_y^2},$$

where the z-axis defines the beam direction.

At a hadron–hadron collider, such as the LHC, the collisions take place in the centre-of-mass frame of the pp system, which is not the centre-of-mass frame of the colliding partons. The net longitudinal momentum of the colliding parton–parton system is given by $(x_1 - x_2)E_p$, where E_p is the energy of the proton. Consequently, in a process such pp $\rightarrow$ 2 jets + X, the two final-state jets are boosted along the beam direction. For this reason, the jet angles are usually expressed in terms of the rapidity y, defined by

$$y = \frac{1}{2} \ln\left(\frac{E + p_z}{E - p_z}\right), \tag{10.41}$$

where E and p_z are the measured energy and z-component of momentum of a jet. The use of rapidity has the advantage that rapidity differences are invariant under boosts along the beam direction. This can be seen by considering the effect of a Lorentz transformation along the z-axis, where the rapidity y in the boosted frame of reference is given by

$$\begin{aligned} y' &= \frac{1}{2} \ln\left[\frac{E' + p'_z}{E' - p'_z}\right] = \frac{1}{2} \ln\left[\frac{\gamma(E - \beta p_z) + \gamma(p_z - \beta E)}{\gamma(E - \beta p_z) - \gamma(p_z - \beta E)}\right] \\ &= \frac{1}{2} \ln\left[\frac{(1-\beta)(E + p_z)}{(1+\beta)(E - p_z)}\right] \\ &= y + \frac{1}{2} \ln\left(\frac{1-\beta}{1+\beta}\right). \end{aligned}$$

Hence, differences in rapidities are the same measured in any two frames, $\Delta y' = \Delta y$. Therefore, the *a priori* unknown longitudinal boost of the parton–parton system does not affect the distribution of rapidity differences.

The invariant mass of the system of particles forming a jet is referred to as the jet mass. The jet mass is not the same as the mass of the primary parton; it is mainly generated in the hadronisation process. For high-energy jets, the jet mass is usually small compared to the jet energy and $p_z \approx E \cos\theta$, where θ is the polar angle of the jet with respect to the beam axis. Hence the rapidity can be approximated by

$$y \approx \frac{1}{2} \ln\left(\frac{1 + \cos\theta}{1 - \cos\theta}\right) = \frac{1}{2} \ln\left(\cot^2 \tfrac{\theta}{2}\right).$$

Therefore, the pseudorapidity η defined as

$$\eta \equiv -\ln\left(\tan \tfrac{\theta}{2}\right)$$

can be used in place of rapidity y when jet masses can be neglected. Figure 10.27 illustrates the polar angle ranges covered by different regions of pseudorapidity.

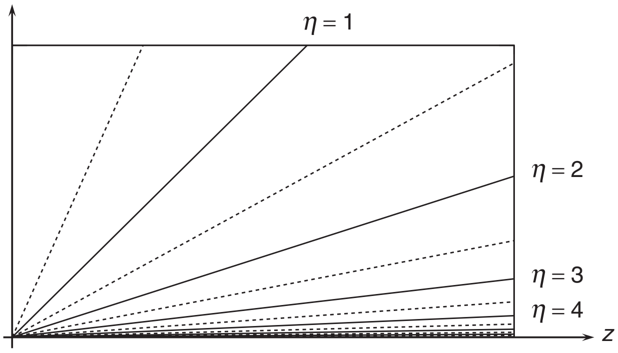

Fig. 10.27 Pseudorapidity regions relative to the beam axis (z).

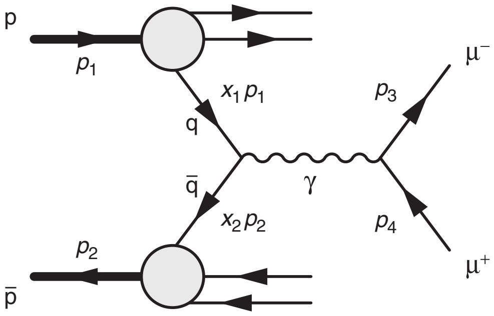

Fig. 10.28 The lowest-order Feynman diagram for the Drell–Yan process $p\bar{p} \to \mu^+\mu^- X$.

Broadly speaking, the differential cross sections for jet production in hadron–hadron collisions are approximately constant in pseudorapidity, implying that roughly equal numbers of jets are observed in each interval of pseudorapidity shown in Figure 10.27, reflecting the forward nature of jet production in pp and $p\bar{p}$ collisions.

10.9.2 The Drell–Yan process

The QED production of a pair of leptons in hadron–hadron collisions from the annihilation of an antiquark and a quark, shown in Figure 10.28, is known as the Drell–Yan process. It provides a useful example of a cross section calculation for hadron–hadron collisions, in this case $p\bar{p} \to \mu^+\mu^- X$, where X represents the remnants of the colliding hadrons.

The QED annihilation cross section for $e^+e^- \to \mu^+\mu^-$ was calculated in Chapter 7. The corresponding cross section for $q\bar{q} \to \mu^+\mu^-$ annihilation is

$$\sigma(q\bar{q} \to \mu^+\mu^-) = \frac{1}{N_c} Q_q^2 \frac{4\pi\alpha^2}{3\hat{s}}, \tag{10.42}$$

where Q_q is the quark/antiquark charge and $\hat{s}$ is the centre-of-mass energy of the colliding $q\bar{q}$ system. The factor $1/N_c$, where $N_c = 3$ is the number of colours, accounts for the conservation of colour charge, which implies that of the nine possible colour combinations of the $q\overline{q}$ system, the annihilation process can only occur for three, $r\overline{r}$, $b\overline{b}$ and $g\overline{g}$. From the definition of the parton distribution functions, the contribution to the $p\overline{p}$ Drell–Yan cross section from an up-quark within the proton with momentum fraction $x_1 \to x_1 + \delta x_1$ annihilating with an anti-up-quark within the antiproton with momentum fraction $x_2 \to x_2 + \delta x_2$ is

$$d^2\sigma = Q_u^2 \frac{4\pi\alpha^2}{9\hat{s}} u^p(x_1)dx_1\, \overline{u}^{\overline{p}}(x_2)\, dx_2, \tag{10.43}$$

where $\overline{u}^{\overline{p}}(x_2)$ is the PDF for the anti-up-quark in the antiproton. Because the antiquark PDFs within the antiproton will be identical to the corresponding quark PDFs in the proton, $\overline{u}^{\overline{p}}(x) = u^p(x) \equiv u(x)$, Equation (10.43) can be written

$$d^2\sigma = \frac{4}{9} \cdot \frac{4\pi\alpha^2}{9\hat{s}} u(x_1)u(x_2)\, dx_1 dx_2. \tag{10.44}$$

The centre-of-mass energy of the $q\overline{q}$ system can be expressed in terms of that of the proton–antiproton system using

$$\hat{s} = (x_1 p_1 + x_2 p_2)^2 = x_1^2 p_1^2 + x_2^2 p_2^2 + 2x_1 x_2 p_1 \cdot p_2.$$

In the high-energy limit, where the proton mass squared can be neglected, $p_1^2 = p_2^2 \approx 0$ and

$$\hat{s} \approx x_1 x_2 (2p_1 \cdot p_2) = x_1 x_2 s,$$

where s is the centre-of-mass energy of the colliding $p\overline{p}$ system. Hence (10.44), expressed in terms of s, becomes

$$d^2\sigma = \frac{4}{9} \cdot \frac{4\pi\alpha^2}{9x_1 x_2 s} u(x_1)u(x_2)\, dx_1 dx_2. \tag{10.45}$$

Accounting for the (smaller) contribution from the annihilation of a $\overline{u}$ in the proton with a u in the antiproton and the contribution from $d\overline{d}$ annihilation, leads to

$$d^2\sigma = \frac{4\pi\alpha^2}{9x_1 x_2 s}\left[\tfrac{4}{9}\left\{u(x_1)u(x_2) + \overline{u}(x_1)\overline{u}(x_2)\right\} + \tfrac{1}{9}\left\{d(x_1)d(x_2) + \overline{d}(x_1)\overline{d}(x_2)\right\}\right] dx_1 dx_2. \tag{10.46}$$

The Drell–Yan differential cross section is most usefully expressed in terms of the experimental observables. Here a suitable choice is the rapidity and the invariant mass of the $\mu^+\mu^-$ system, both of which can be determined from the momenta of the μ^+ and μ^- as reconstructed in the tracking system of the detector. The coordinate transformation from x_1 and x_2 to these experimental observables is not entirely straightforward, but is shown to illustrate the general principle. The invariant mass of the $\mu^+\mu^-$ system is equal to the centre-of-mass energy of the colliding partons,

$$M^2 = x_1 x_2 s. \tag{10.47}$$

The rapidity of the $\mu^+\mu^-$ system is given by

$$y = \frac{1}{2}\ln\left(\frac{E_3 + E_4 + p_{3z} + p_{4z}}{E_3 + E_4 - p_{3z} - p_{4z}}\right) = \frac{1}{2}\ln\left(\frac{E_{\mathrm{q}} + E_{\overline{\mathrm{q}}} + p_{\mathrm{q}z} + p_{\overline{\mathrm{q}}z}}{E_{\mathrm{q}} + E_{\overline{\mathrm{q}}} - p_{\mathrm{q}z} - p_{\overline{\mathrm{q}}z}}\right),$$

where the equality of four-momenta of the $\mu^+\mu^-$ system and that of the colliding partons follows from energy and momentum conservation. The four-momenta of the colliding q and $\overline{\mathrm{q}}$ are respectively given by

$$p_{\mathrm{q}} = \frac{\sqrt{s}}{2}(x_1, 0, 0, x_1) \quad \text{and} \quad p_{\overline{\mathrm{q}}} = \frac{\sqrt{s}}{2}(x_2, 0, 0, -x_2),$$

and hence

$$y = \frac{1}{2}\ln\left(\frac{(x_1 + x_2) + (x_1 - x_2)}{(x_1 + x_2) - (x_1 - x_2)}\right) = \frac{1}{2}\ln\frac{x_1}{x_2}. \tag{10.48}$$

From (10.47) and (10.48), x_1 and x_2 can be written in terms of M and y,

$$x_1 = \frac{M}{\sqrt{s}}e^{y} \quad \text{and} \quad x_2 = \frac{M}{\sqrt{s}}e^{-y}. \tag{10.49}$$

The differential cross section in terms of $\mathrm{d}x_1\mathrm{d}x_2$ can be expressed in terms of $\mathrm{d}y\,\mathrm{d}M$ using the determinant of the Jacobian matrix for the coordinate transformation

$$\mathrm{d}y\,\mathrm{d}M = \frac{\partial(y, M)}{\partial(x_1, x_2)}\mathrm{d}x_1\mathrm{d}x_2 = \begin{vmatrix} \frac{\partial y}{\partial x_1} & \frac{\partial y}{\partial x_2} \\ \frac{\partial M}{\partial x_1} & \frac{\partial M}{\partial x_2} \end{vmatrix} \mathrm{d}x_1\,\mathrm{d}x_2,$$

where the partial derivatives obtained from (10.47) and (10.48) give

$$\mathrm{d}y\,\mathrm{d}M = \frac{s}{2M}\mathrm{d}x_1\mathrm{d}x_2.$$

Hence the differential cross section of (10.46) can be expressed as

$$\mathrm{d}^2\sigma = \frac{4\pi\alpha^2}{9M^2}f(x_1, x_2)\frac{2M}{s}\mathrm{d}y\,\mathrm{d}M,$$

where

$$f(x_1, x_2) = \left[\tfrac{4}{9}\left\{u(x_1)u(x_2) + \overline{u}(x_1)\overline{u}(x_2)\right\} + \tfrac{1}{9}\left\{d(x_1)d(x_2) + \overline{d}(x_1)\overline{d}(x_2)\right\}\right],$$

and thus, the Drell–Yan differential cross section, written in terms of the invariant mass and rapidity of the $\mu^+\mu^-$ system, is

$$\frac{\mathrm{d}^2\sigma}{\mathrm{d}y\,\mathrm{d}M} = \frac{8\pi\alpha^2}{9Ms}f(x_1, x_2),$$

where x_1 and x_2 are given by (10.49).

The above treatment of the Drell–Yan process considered only the QED photon-exchange diagram. However, any neutral particle which couples to both quarks and muons can contribute. For example, Figure 10.29 shows the measured differential cross section for $\mathrm{p}\overline{\mathrm{p}} \to \mu^+\mu^- X$ from the CDF experiment at the Tevatron,

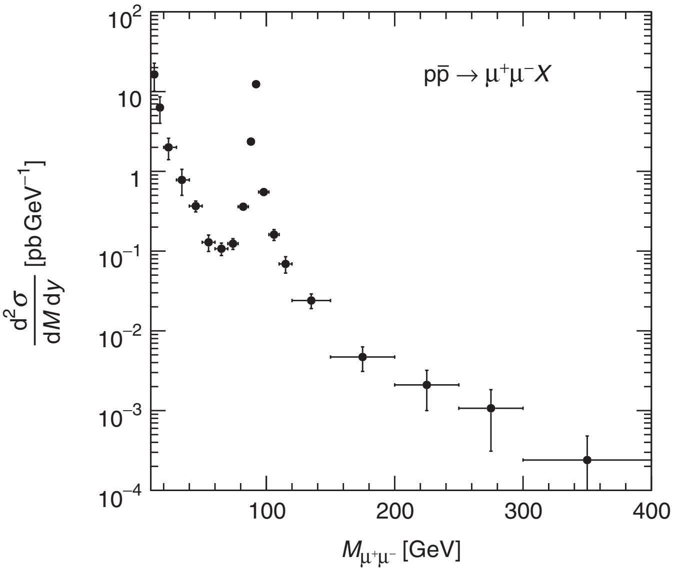

Fig. 10.29 The measured Drell–Yan cross section in $p\bar{p}$ collisions at $\sqrt{s} = 1.8$ TeV in the CDF detector at the Tevatron collider. Adapted from Abe *et al.* (1999).

which operated from 1989 to 2011. The strong enhancement in the cross section at $M_{\mu^+\mu^-} \sim 91$ GeV is due to the resonant production of the Z boson, through the annihilation process $q\bar{q} \to Z \to \mu^+\mu^-$. The Drell–Yan process also provides a way of searching for physics beyond the Standard Model through the production of new massive neutral particles that couple to both quarks and leptons, through the process $q\bar{q} \to X^0 \to \mu^+\mu^-$. To date, no such signals of physics beyond the Standard Model have been observed.

10.9.3 Jet production at the LHC

The Large Hadron Collider at CERN is the highest energy accelerator ever built. It is a pp collider designed to operate at an ultimate centre-of-mass energy of 14 TeV. The LHC commenced full operation at $\sqrt{s} = 7$ TeV in 2010 and ran at $\sqrt{s} = 8$ TeV in 2012. The most common, although not the most interesting, high-energy process at the LHC is the QCD production of two-jets. Figure 10.30 shows an example of a two-jet event recorded at $\sqrt{s} = 7$ TeV in the ATLAS experiment. Since the colliding partons have no momentum transverse to the beam axis, the jets are produce back to back in the transverse plane and have equal and opposite transverse momenta, p_T. In the other view, the jets are not back to back due to the boost of the final-state system from the net momentum of the colliding partons along the beam axis, $(x_1 - x_2)\sqrt{s}/2$.

The cross section for the production of two jets from the t-channel gluon exchange process $qq \to qq$ is given by (10.31),

Fig. 10.30 An example of a pp $\rightarrow$ two-jets X event observed in the ATLAS detector a the LHC: (left) the transverse view (perpendicular to the beam direction) and (right) the yz-view with the z-axis along the beam direction. Reproduced courtesy of the ATLAS collaboration.

$$\frac{\mathrm{d}\sigma}{\mathrm{d}Q^2} = \frac{4\pi\alpha_S^2}{9Q^4}\left[1 + \left(1 - \frac{Q^2}{\hat{s}}\right)^2\right],$$

where $Q^2 = -q^2$ and $\hat{s} = x_1 x_2 s$ is the centre-of-mass energy of the colliding quarks. The contribution to the proton–proton cross section, expressed in terms of the parton density functions, is therefore

$$\frac{\mathrm{d}\sigma}{\mathrm{d}Q^2} = \frac{4\pi\alpha_S^2}{9Q^4}\left[1 + \left(1 - \frac{Q^2}{s x_1 x_2}\right)^2\right] g(x_1, x_2)\,\mathrm{d}x_1\mathrm{d}x_2.$$

where $g(x_1, x_2)$ is the sum over the products of the relevant parton distribution functions for the scattering process qq → qq, which for up- and down-quarks is

$$g(x_1, x_2) = [u(x_1)u(x_2) + u(x_1)d(x_2) + d(x_1)u(x_2) + d(x_1)d(x_2)]\,.$$

The differential cross section therefore can be written as

$$\frac{\mathrm{d}^3\sigma}{\mathrm{d}Q^2\,\mathrm{d}x_1\,\mathrm{d}x_2} = \frac{4\pi\alpha_S^2}{9Q^4}\left[1 + \left(1 - \frac{Q^2}{s x_1 x_2}\right)^2\right] g(x_1, x_2). \tag{10.50}$$

This expression has three degrees of freedom; one from the underlying elastic scattering process, here written in terms of Q^2, and one from each of the parton momentum fractions, x_1 and x_2. In the process pp → two-jets X, the experimentally well-measured quantities are the rapidities of the two final-state jets, y_3 and y_4, and the magnitude of the transverse momentum, p_T (which is the same for both jets). Equation (10.50) can be written in terms of these measured quantities using the determinant of the Jacobian for the coordinate transformation from $\{Q^2, x_1, x_2\}$ to $\{p_\mathrm{T}, y_3, y_4\}$ (see Problems 10.6 and 10.7). In principle, given knowledge of the PDFs, it would be possible to calculate the lowest-order QCD contribution to the LHC two-jet production cross section from the process qq → qq and express it in terms of these three experimental observables. However, qq → qq is just one of a number of parton-level processes that contribute to pp → two-jets X at the LHC. For example, some of the other Feynman diagrams resulting in a two-jet

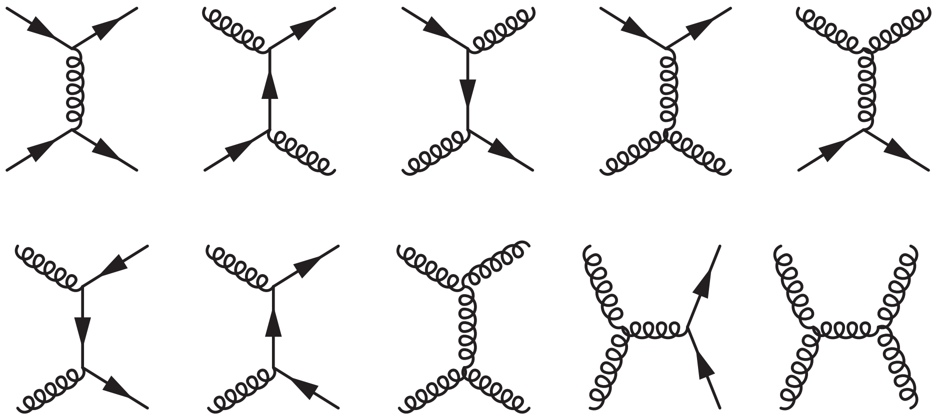

Fig. 10.31 Feynman diagrams for two-jet production in proton–proton collisions. There are also diagrams involving initial-state antiquarks.

final state are shown in Figure 10.31. The contributions from all processes, including the interference between diagrams with the same final-state partons, need to be summed to obtain the cross section for pp → two-jets X. Furthermore, for accurate predictions, the effects of higher-order QCD diagrams also need to be considered.

At this point, it should be clear that unlike the case of electron–positron annihilation, cross section calculations for the LHC are highly complex. Not only are the PDFs required, but multiple diagrams are involved and higher orders have to be included. In practice, such calculations are performed numerically in highly sophisticated computer programs. Nevertheless, the comparison of the predictions from these calculations with the experimental data from the LHC provides a powerful test of QCD. For example, Figure 10.32 shows early data from the CMS experiment. The plot shows the inclusive jet production cross section $\mathrm{d}^2\sigma/\mathrm{d}p_\mathrm{T}\mathrm{d}y$ in intervals of $\Delta y = 0.5$ of rapidity (which correspond to different ranges of polar angles in the detector). The p_T distribution is peaked towards zero, reflecting the $1/Q^4$ propagator term and the large values of the PDFs at low x. The measured cross sections for each interval of rapidity are similar, with roughly equal numbers of jets being observed in each of the (pseudo)rapidity intervals shown in Figure 10.27, demonstrating that jets are produced preferentially in the forward directions.

The data of Figure 10.32 are compared to next-to-leading-order (NLO) QCD predictions using the current knowledge of the PDFs. The predicted cross sections are in good agreement with the data that span a wide range of jet p_T. In general, QCD is found to provide an excellent description of jet phenomena in hadron–hadron collisions. The success of QCD in describing the experimental results is an important achievement of modern particle physics and provides overwhelming evidence for the existence of the underlying SU(3) gauge symmetry.

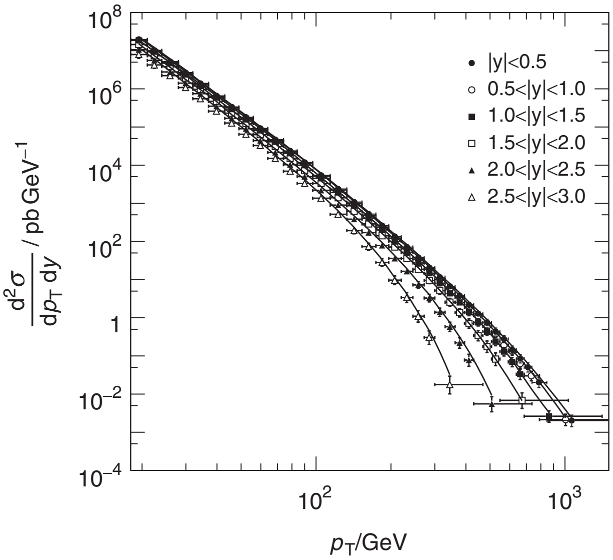

Fig. 10.32 The measurement of the inclusive differential cross section for jet production from data recorded at $\sqrt{s} = 7$ TeV in the CMS experiment at the LHC. The curves are the predicted cross sections from NLO QCD. Adapted from Chatrchyan *et al.* (2011).

Summary

Quantum Chromodynamics is the quantum field theory of the strong interaction. It corresponds to a non-Abelian SU(3) local gauge symmetry, with eight gluons associated with the eight generators. The interactions between the gluons and quarks are described by the qqg vertex factor

$$-\tfrac{1}{2}ig_S\lambda^a_{ji}\gamma^\mu,$$

where i and j are the colour charges of the quarks. The corresponding Feynman rule for the gluon propagator is

$$-i\frac{g_{\mu\nu}}{q^2}\delta^{ab}.$$

Whilst the Feynman rules for the QCD vertex and the gluon propagator resemble those of QED, the presence of gluon self-interactions leads to very different behaviour. For example, colour is confined and all freely propagating particles are colour singlet states; free quarks and gluons are not observed.

The running of $\alpha_S(Q^2)$ implies that the strength of the QCD interaction decreases with energy scale, a property known as asymptotic freedom. As a consequence, perturbative calculations can be used for high-energy QCD processes. Despite the practical difficulties of performing accurate calculations, QCD is found to provide an excellent description of hadron collider data and the SU(3) local gauge symmetry should be considered to be an experimentally established fact.

Problems

10.1 By considering the symmetry of the wavefunction, explain why the existence of the $\Omega^-(\mathrm{sss})$ $L = 0$ baryon provides evidence for a degree of freedom in addition to space × spin × flavour.

10.2 From the expression for the running of α_S with $N_f = 3$, determine the value of q^2 at which α_S appears to become infinite. Comment on this result.

10.3 Find the overall "colour factor" for $\mathrm{qq} \rightarrow \mathrm{qq}$ if QCD corresponded to a SU(2) colour symmetry.

10.4 Calculate the non-relativistic QCD potential between quarks q_1 and q_2 in a $\mathrm{q}_1\mathrm{q}_2\mathrm{q}_3$ baryon with colour wavefunction

$$\psi = \frac{1}{\sqrt{6}}(rgb - grb + gbr - bgr + brg - rbg).$$

10.5 Draw the lowest-order QCD Feynman diagrams for the process $\mathrm{p}\overline{\mathrm{p}} \rightarrow$ two-jets $+ X$, where X represents the remnants of the colliding hadrons.

10.6 The observed events in the process $\mathrm{pp} \rightarrow$ two-jets at the LHC can be described in terms of the jet p_T and the jet rapidities y_3 and y_4.

(a) Assuming that the jets are massless, $E^2 = p_\mathrm{T}^2 + p_z^2$, show that the four-momenta of the final-state jets can be written as

$$\begin{aligned} p_3 &= (p_\mathrm{T}\cosh y_3, +p_\mathrm{T}\sin\phi, +p_\mathrm{T}\cos\phi, p_\mathrm{T}\sinh y_3), \\ p_4 &= (p_\mathrm{T}\cosh y_4, -p_\mathrm{T}\sin\phi, -p_\mathrm{T}\cos\phi, p_\mathrm{T}\sinh y_4). \end{aligned}$$

(b) By writing the four-momenta of the colliding partons in a pp collision as

$$p_1 = \frac{\sqrt{s}}{2}(x_1, 0, 0, x_1) \quad \text{and} \quad p_2 = \frac{\sqrt{s}}{2}(x_2, 0, 0, -x_1),$$

show that conservation of energy and momentum implies

$$x_1 = \frac{p_\mathrm{T}}{\sqrt{s}}(e^{+y_3} + e^{+y_4}) \quad \text{and} \quad x_2 = \frac{p_\mathrm{T}}{\sqrt{s}}(e^{-y_3} + e^{-y_4}).$$

(c) Hence show that

$$Q^2 = p_\mathrm{T}^2(1 + e^{y_4 - y_3}).$$

10.7 Using the results of the previous question show that the Jacobian

$$\frac{\partial(y_3, y_4, p_\mathrm{T}^2)}{\partial(x_1, x_2, q^2)} = \frac{1}{x_1 x_2}.$$

10.8 The total cross section for the Drell–Yan process $p\bar{p} \rightarrow \mu^+\mu^- X$ was shown to be

$$\sigma_{DY} = \frac{4\pi\alpha^2}{81s}\int_0^1\int_0^1 \frac{1}{x_1x_2}\left[4u(x_1)u(x_2) + 4\bar{u}(x_1)\bar{u}(x_2) + d(x_1)d(x_2) + \bar{d}(x_1)\bar{d}(x_2)\right] dx_1 dx_2 \, .$$

(a) Express this cross section in terms of the valence quark PDFs and a single PDF for the sea contribution, where $S(x) = \bar{u}(x) = \bar{d}(x)$.

(b) Obtain the corresponding expression for $pp \rightarrow \mu^+\mu^- X$.

(c) Sketch the region in the x_1–x_2 plane corresponding $s_{q\bar{q}} > s/4$. Comment on the expected ratio of the Drell–Yan cross sections in pp and $p\bar{p}$ collisions (at the same centre-of-mass energy) for the two cases: (i) $\hat{s} \ll s$ and (ii) $\hat{s} > s/4$, where $\hat{s}$ is the centre-of-mass energy of the colliding partons.

10.9 Drell–Yan production of $\mu^+\mu^-$-pairs with an invariant mass Q^2 has been studied in $\pi^\pm$ interactions with carbon (which has equal numbers of protons and neutrons). Explain why the ratio

$$\frac{\sigma(\pi^+ C \rightarrow \mu^+\mu^- X)}{\sigma(\pi^- C \rightarrow \mu^+\mu^- X)}$$

tends to unity for small Q^2 and tends to $\frac{1}{4}$ as Q^2 approaches s.